

1 **Estimating the lateral transfer of organic carbon through the European river**
2 **network using a land surface model**

3 Haicheng Zhang^{1*}, Ronny Lauerwald², Pierre Regnier¹, Philippe Ciais³, Kristof Van Oost⁴,
4 Victoria Naipal⁵, Bertrand Guenet³, Wenping Yuan⁶

5 ¹Department Geoscience, Environment & Society-BGEOSYS, Université libre de Bruxelles, 1050 Bruxelles,
6 Belgium

7 ² Université Paris-Saclay, INRAE, AgroParisTech, UMR ECOSYS, 78850, Thiverval-Grignon, France

8 ³Laboratoire des Sciences du Climat et de l'Environnement, IPSL-LSCE CEA/CNRS/UVSQ, Orme des Merisiers,
9 91191, Gif sur Yvette, France

10 ⁴UCLouvain, TECLIM - Georges Lemaître Centre for Earth and Climate Research, Louvain-la-Neuve, Belgium

11 ⁵EcoAct/ ATOS, 35 rue de miromesnil, 75008, Paris, France

12 ⁶School of Atmospheric Science, Sun Yat-sen University, Guangzhou, Guangdong, 510275, China

13

14 *Correspondence to:* Haicheng Zhang (haicheng.zhang@ulb.be)

15 **Abstract.** Lateral carbon transport from soils to the ocean through rivers has been acknowledged
16 as a key component of global carbon cycle, but is still neglected in most global land surface
17 models (LSMs). Fluvial transport of dissolved organic carbon (DOC) and CO₂ has been
18 implemented in the ORCHIDEE LSM, while erosion-induced delivery of sediment and
19 particulate organic carbon (POC) from land to river was implemented in another version of the
20 model. Based on these two developments, we take the final step towards the full representation
21 of biospheric carbon transport through the land-river continuum. The newly developed model,
22 called ORCHIDEE-C_{lateral}, simulates the complete lateral transport of water, sediment, POC,
23 DOC and CO₂ from land to sea through the river network, the deposition of sediment and POC in
24 the river channel and floodplains, and the decomposition of POC and DOC in transit. We
25 parameterized and evaluated ORCHIDEE-C_{lateral} using observation data in Europe. The model
26 explains 94%, 75% and 83% of the spatial variations of observed riverine water discharges,
27 bankfull water flows and riverine sediment discharges in Europe, respectively. The simulated
28 long-term average total organic carbon concentrations and DOC concentrations in river flows are
29 comparable to the observations in major European rivers, although our model generally
30 overestimates the seasonal variation of riverine organic carbon concentrations. Application of
31 ORCHIDEE-C_{lateral} for Europe reveals that the lateral carbon transfer affects land carbon
32 dynamics in multiple ways and omission of this process in LSMs may lead to an overestimation of
33 4.5% in the simulated annual net terrestrial carbon uptake over Europe. Overall, this study presents a
34 useful tool for simulating large scale lateral carbon transfer and for predicting the feedbacks
35 between lateral carbon transfer and future climate and land use changes.

36 **1 Introduction**

37 Lateral transfer of organic carbon along the land-river-ocean continuums, involving both spatial
38 redistribution of terrestrial organic carbon and the vertical land-atmosphere carbon exchange, has
39 been acknowledged as a key component of the global carbon cycle (Ciais et al., 2013; Ciais et
40 al., 2021; Drake et al., 2018; Regnier et al., 2013). Erosion of soils and the associated organic
41 carbon, but also leaching of soil dissolved organic carbon (DOC), represent a non-negligible leak
42 in the terrestrial carbon budget and a substantial source of allochthonous organic carbon to
43 inland waters and oceans (Battin et al., 2009; Cole et al., 2007; Raymond et al., 2013; Regnier et
44 al., 2013). As a result of soil aggregate breakdown and desorption, the accelerated mineralization
45 of these eroded and leached soil carbon loads leads to considerable CO₂ emission to the
46 atmosphere (Chappell et al., 2016; Lal, 2003; Van Hemelryck et al., 2011). Meanwhile, the
47 organic carbon that is redeposited and buried in floodplains and lakes might be preserved for a
48 long time, thus creating a CO₂ sink (Stallard, 1998; Van Oost et al., 2007; Wang et al., 2010;
49 Hoffmann, 2022). In addition, lateral redistribution of soil material can alter land-atmosphere
50 CO₂ fluxes indirectly by affecting soil nutrient availability, terrestrial vegetation productivity and
51 physiochemical properties of inland and coastal waters (Beusen et al., 2005; Vigiak et al., 2017).

52 Although the important role of lateral carbon transfer in the global carbon cycle has been widely
53 recognized, to date, the estimates of land carbon loss to inland waters, the fate of the terrestrial
54 organic carbon within inland waters, as well as the net effect of lateral carbon transfer on land-
55 atmosphere CO₂ fluxes remain largely uncertain (Berhe et al., 2007; Doetterl et al., 2016; Lal,
56 2003; Stallard, 1998; Wang et al., 2014b; Zhang et al., 2014). Existing estimates of global carbon
57 loss from soils to inland waters vary from 1.1 to 5.1 Pg (=10¹⁵ g) C per year (yr⁻¹) (Cole et al.,
58 2007; Drake et al., 2018), and the estimated net impact of global lateral carbon redistribution on
59 land-atmosphere carbon budget ranges from an uptake of atmospheric CO₂ by 1 Pg C yr⁻¹ to a
60 land CO₂ emission of 1 Pg C yr⁻¹ (Lal, 2003; Stallard, 1998; Van Oost et al., 2007; Wang et al.,
61 2017). A reliable model which is able to explicitly simulate the lateral carbon flux along the
62 land-river continuum and also the interactions between these lateral fluxes and the
63 comprehensive terrestrial carbon cycle, would thus be necessary for projecting changes in the
64 global carbon cycle more accurately.

65 Global land surface models (LSMs) are important tools to simulate the feedbacks between
66 terrestrial carbon cycle, increasing atmospheric CO₂, and climate and land use change. However,
67 the lateral carbon transfer, especially for the particulate organic carbon (POC), is still missing or
68 incompletely represented in existing LSMs (Lauerwald et al., 2017; Lauerwald et al., 2020;
69 Lugato et al., 2016; Naipal et al., 2020; Nakhavali et al., 2021; Tian et al., 2015). It has been
70 hypothesized that the exclusion of lateral carbon transfer in LSMs implies a significant bias in
71 the simulated global land carbon budget (Ciais et al., 2013; Ciais et al., 2021; Janssens et al.,
72 2003). For instance, the study of Nakhavali et al. (2021) suggested that about 15% of the global
73 terrestrial net ecosystem production is exported to inland waters as leached DOC. Lauerwald et
74 al. (2020) showed that the omission of lateral DOC transfer in LSM might lead to significant
75 underestimation (8.6%) of the net uptake of atmospheric carbon in the Amazon basin while
76 terrestrial carbon storage changes in response to the increasing atmospheric CO₂ concentrations
77 were overestimated.

78 Over the past decade, a number of LSMs have been developed which represent leaching of DOC
79 from soils (Nakhavali et al. 2018, Kicklighter et al. 2013) or the full transport of DOC through
80 the land-river continuum (Lauerwald et al., 2017; Tian et al., 2015). However, the erosion-
81 induced transport of soil POC, which has also been reported to be able to affect the carbon
82 balance of terrestrial ecosystems strongly (Lal., 2003; Van Oost et al., 2007; Tian et al., 2015), is
83 still not or poorly represented in LSMs. The explicit simulation of the complete transport process
84 of POC at large spatial scales is still a major challenge, due to the complexity of the processes
85 involved, including erosion-induced sediment and POC delivery to rivers, deposition of
86 sediment and POC in river channels and floodplains, re-detachment of the previously deposited
87 sediments and POC, decomposition and transformation of POC in riverine and flooding waters,
88 as well as the changes of soil profile caused by erosion and deposition (Doetterl et al., 2016;
89 Naipal et al., 2020; Zhang et al., 2020).

90 Several recent model developments have led to the implementation of the lateral transfer of POC
91 in large-scale LSMs. Despite this, there are still some inevitable limitations in these
92 implementations. The Dynamic Land Ecosystem Model (DLEM v2.0, Tian et al., 2015) is able
93 to simulate the erosion-induced POC loss from soil to river and the transport and decomposition
94 of POC in river networks. However, it does not represent the POC deposition in floodplains, nor

95 the impacts of soil erosion and floodplain deposition on the vertical profiles of soil organic
96 carbon (SOC). The Carbon Erosion DYNAMics model (CE-DYNAM, Naipal et al., 2020)
97 simulates erosion of SOC and its re-deposition on the toe-slope or floodplains, transport of POC
98 along river channels, as well as the impact on SOC dynamics at the eroding and deposition sites.
99 However, running at annual time scale, it mostly addresses the centennial timescale and does not
100 represent deposition and decomposition of POC in river channels. Moreover, CE-DYNAM was
101 only applied over the Rhine catchment and has not been fully coupled into a land surface model,
102 therefore excluding the feedbacks of soil erosion on the fully coupled land and aquatic carbon
103 cycles. There are of course more dedicated hydrology and soil erosion models that explicitly
104 simulate the complete transport, deposition and decomposition processes of POC in small river
105 basins (e.g. Jetten et al., 2003; Nearing et al., 1989; Neitsch et al., 2011). However, it is difficult
106 to apply these models at large spatial scales (e.g. continental or global scale) due to the limited
107 availability of forcing data (e.g. geometric attributes of river channel), suitable model
108 parameterization and computational capacity. Moreover, these models have limited capability of
109 representing the full terrestrial C cycle in response to climate change, increasing atmospheric
110 CO₂ and land use change. Therefore, basin-scale models are not an option to assess the impact of
111 soil erosion on the large-scale terrestrial C budget in response to global changes.

112 Here we describe the development, application and evaluation of a new branch of the
113 ORCHIDEE LSM (Krinner et al., 2005), hereafter ORCHIDEE-C_{lateral}, that can be used to
114 simulate the complete lateral transfer processes of water, sediment, POC and DOC along the
115 land-river-ocean continuum at large spatial scale (e.g. continental and global scale). In previous
116 studies, the leaching and fluvial transfer of DOC and the erosion-induced delivery of sediment
117 and POC from upland soil to river network have been implemented in two different branches of
118 the ORCHIDEE LSM (i.e. ORCHILEAK (Lauerwald et al., 2017) and ORCHIDEE-MUSLE
119 (Zhang et al., 2020)). For this new branch, we first merged these two branches, and subsequently
120 implemented the fluvial transfer of sediment and POC in the coupled model. ORCHIDEE-C_{lateral}
121 is calibrated and evaluated using observation data of runoff, bankfull flow, and riverine loads and
122 concentrations of sediment, POC and DOC across Europe. By applying the calibrated model at
123 European scale, we estimate the magnitude and spatial distribution of the lateral carbon transfer
124 in European catchments during the period 1901-2014, as well as the potential impacts of lateral
125 carbon transfer on the land carbon balance. Comparing simulations results to those of an

126 alternative simulation run with lateral displacement of C deactivated, we finally quantify the
127 biases in simulated land C budgets that arise ignoring the lateral transfers of C along the land-
128 river continuum.

129

130 **2 Model development and evaluation**

131 **2.1 ORCHIDEE land surface model**

132 The ORCHIDEE LSM comprehensively simulates the cycling of energy, water and carbon in
133 terrestrial ecosystems (Krinner et al., 2005). The hydrological processes (e.g. rainfall
134 interception, evapotranspiration and soil water dynamics) and plant photosynthesis in
135 ORCHIDEE are simulated at a time step of 30 minutes. The carbon cycle processes (e.g.
136 maintenance and growth respiration, carbon allocation, litter decomposition, SOC dynamics,
137 plant phenology and mortality) are simulated at daily time step. In its default configuration,
138 ORCHIDEE represents 13 land cover types, with one for bare soil and 12 for lands covered by
139 vegetation (eight types of forests, two types of grasslands, two types of croplands). Given
140 appropriate land cover maps and parametrization, the number of PFTs to be represented can
141 however be adapted (Zhang et al., 2020).

142 Our previous implementations of lateral DOC transfer (Lauerwald et al., 2017) and of POC
143 delivery from upland to river network (Zhang et al., 2020) were both based on the ORCHIDEE
144 branch ORCHIDEE-SOM (Camino-Serrano et al., 2018, Fig. S1), which provides a depth-
145 dependent description of the water and carbon dynamics in soil column. In specific, the vertical
146 soil profile in ORCHIDEE-SOM is described by an 11-layer discretization of a 2 m soil column
147 (Camino-Serrano et al., 2018). Water flows between adjacent soil layers are simulated using the
148 Fokker–Planck equation that resolves water diffusion in non-saturated conditions (Campoy et al.,
149 2013; Guimberteau et al., 2018). Free gravitational drainage occurs in the lowest soil layer when
150 actual soil water content is higher than the residual water content (Campoy et al., 2013).
151 Following the CENTURY model (Parton et al., 1988), ORCHIDEE-SOM represents two litter
152 pools (metabolic and structural) and three SOC pools (active, slow and passive) that differ in
153 their respective turnover times. The decomposition of each carbon pool is calculated by first
154 order kinetics based on the corresponding turnover time, soil moisture and temperature as

155 controlling factors, as well as the priming effects of fresh organic matter (Guenet et al., 2018;
156 Guenet et al., 2016). Soil DOC is represented by a labile and a stable DOC pools, with a high
157 and low turnover rate, respectively. Each DOC pool may be in the soil solution or adsorbed on
158 the mineral matrix. The products of litter and SOC decomposition enter free DOC pool, which in
159 turn is decomposed following first order kinetics (Kalbitz et al., 2003) and returns back to SOC.
160 Adsorption and desorption of DOC follows an equilibrium distribution coefficient calculated
161 from soil clay and pH. Free DOC can be transported with the water flux simulated by the soil
162 hydrological module of ORCHIDEE. However, DOC adsorbed to soil minerals can neither be
163 decomposed nor transported (Camino-Serrano et al., 2018). All the described processes occur
164 within each soil layer. At each time step, “the flux of DOC leaving the soil is calculated by
165 multiplying DOC concentrations in soil solution with the runoff (surface layer) and drainage
166 (bottom layer) flux simulated by the hydrological module” (Camino-Serrano et al., 2018, p. 939).
167 More detailed information about the simulation of soil hydrological and biogeochemical
168 processes in ORCHIDEE-SOM can be found in Guenet et al. (2016) and Camino-Serrano et al.
169 (2018).

170 **2.1.1 Lateral transfer of DOC and CO₂**

171 Lateral transfer of DOC and dissolved CO₂ from land to ocean through river network has been
172 implemented in the ORCHILEAK (Lauerwald et al., 2017), an ORCHIDEE branch developed
173 from ORCHIDEE-SOM (Fig. S1). The adsorption, desorption, production, consumption and
174 transport of DOC within the soil column, as well as DOC export from soil to river along with
175 surface runoff and drainage in ORCHILEAK is simulated using the same method as
176 ORCHIDEE-SOM. Besides the decomposition of SOC and litter, ORCHILEAK also represents
177 the contribution of wet and dry deposition to soil DOC via throughfall. The direct DOC input
178 from rainfall to aquatic DOC pools is simulated based on the DOC concentration in rainfall and
179 the area fraction of stream and flooding waters in each basin. Simulation of the lateral transfer of
180 DOC and CO₂ in river networks, i.e. the transfer of DOC and CO₂ from one basin to another
181 based on the stream flow directions obtained from a forcing file (0.5°, Table 1), follows the
182 routing scheme of water (Guimberteau et al., 2012). For each basin with floodplain (defined by
183 forcing data), bankfull flow occurs when stream volume in the river channel exceeds a threshold
184 prescribed by the forcing file (Table 1). DOC and CO₂ in flooding waters can enter into soil

185 DOC and CO₂ pools along with the infiltrating water. On the contrary, DOC and CO₂ originated
 186 from the decomposition of submerged litter and SOC in the floodplains are added to the
 187 overlying flooding waters. Note that the turnover times of litter and SOC under flooding waters
 188 are assumed to be three times of the litter and SOC turnover times in upland soil (Reddy &
 189 Patrick Jr, 1975; Neckles & Neill, 1994; Lauerwald et al., 2017). After removing the infiltrated
 190 and evaporated water, the amount of the remaining flooding water, as well as the DOC and
 191 dissolved CO₂ returning to river channel at the end of each day is calculated based on a time
 192 constant of flooding water (= 4.0 days, d'Orgeval et al., 2008) modified by a basin-specific
 193 topographic index (f_{topo} , unitless) (Lauerwald et al., 2017).

194

195 **Table 1.** List of forcing data needed to run ORCHIDEE-C_{lateral} and the data used to evaluate the
 196 simulation results. S_{res} and T_{res} are the spatial and temporal resolution of the forcing data,
 197 respectively.

	Data	S_{res}	T_{res}	Data source
Forcing	Climatic forcing data (precipitation, temperature, incoming shortwave/longwave radiation, air pressure, wind speed, relative humidity)	0.5°	3 hour	GSWP3 database (Dirmeyerm et al., 2006)
	Land cover	0.5°	1 year	LUHa.rc2 database (Chini et al., 2014)
	Soil texture class	0.5°	–	Reynolds et al. (1999)
	Soil bulk density and pH	30"	–	HWSD v1.2 (FAO/IIASA/ISRIC/ISSCAS/JRC, 2012)
	Stream flow directions, topographic index (f_{topo})	0.5°	–	STN-30p (Vörösmarty et al., 2000)
	Area fraction of floodplains	250 m	–	GFPLAIN250m (Nardi et al., 2019) ^a
	Area fraction of river surface	0.5°	–	Lauerwald et al. (2015)
	Maximum water storage in river channel (S_{rivmax})	0.5°	–	Derived from pre-runs with ORCHIDEE-C _{lateral} (see section 2.3)
	Reference sediment delivery rate (SED_{ref})	0.5°	–	Zhang et al. (2020)
	Digital Elevation Model (DEM)	3"	–	HydroSHEDS (Lehner et al., 2008) and GDEM v3 (Abrams et al., 2020) ^b
Val	Riverine water discharge	–	1 day	GRDC ^c

Bankfull flow	–	1 year	Schneider et al. (2011)
Sediment delivery from upland to inland waters	100 m	1 year	Borrelli et al. (2018)
Riverine sediment discharge	–	1 year	European Environment Agency ^d and publications ^e
Riverine POC and DOC concentration	–	Instantaneous	GLORICH (Hartmann et al., 2019)
	30"		HWSD v1.2
	5'		GSDE (Shangguan et al., 2014)
SOC stock	250 m	–	SoilGrids (Hengl et al., 2014)
	10 km		S2017 (Sanderman et al., 2017)
	250 m		LandGIS ^f

198 ^a The GFPLAIN250m only covers the regions south of 60° N. We produced map of floodplain distribution in
199 regions north of the 60° N using the same method for producing GFPLAIN250m (Nardi et al., 2019) based on the
200 ASTER GDEM v3 database (Abrams et al., 2020). ^b The DEM data from HydroSHEDS and GDEM v3 are used to
201 extract the topographic properties (e.g. location, area and average slope) of headwater basins in regions south and
202 north of 60° N, respectively. ^c The Global Runoff Data Centre, 56068 Koblenz, Germany. ^d
203 <https://www.eea.europa.eu/data-and-maps/data/sediment-discharges>. ^e Publications including Van Dijk & Kwaad,
204 1998; Vollmer & Goelz, (2006) and Reports of the DanubeSediment project (Sediment Management Measures for
205 the Danube, <http://www.interreg-danube.eu/approved-projects/danubeseiment>). ^f
206 <https://zenodo.org/record/2536040#.Yc-QGo9KiUm>.

207

208 Decomposition of DOC in stream and flooding waters is calculated at daily time step based on
209 the prescribed turnover times of labile (2 days) and refractory (80 days) DOC in waters (when
210 temperature is 28 °C) and a temperature factor obtained from Hanson et al. (2011). CO₂ evasion
211 in inland waters is simulated using a much fine integration time step of 6 minutes. The CO₂
212 partial pressures (*p*CO₂) in water column is first calculated based on the temperature-dependent
213 solubility of CO₂ and the concentration of dissolved CO₂ (Telmer and Veizer, 1999). Then the
214 CO₂ evasion is calculated based on the gas exchange velocity, the water–air gradient in *p*CO₂,
215 and the surface water area available for gas exchange (Lauerwald et al., 2017). In addition,
216 swamp and wetland are also represented in the routing scheme of ORCHILEAK. More detailed
217 descriptions can be found in Lauerwald et al. (2017).

218 **2.1.2 Sediment and particulate organic carbon delivery from upland soil to river network**

219 To give an accurate simulation of sediment delivery from uplands to river network and maintain
 220 computational efficiency, an upscaling scheme which integrates information from high-resolution (3")
 221 topographic and soil erodibility data into a LSM forcing file at 0.5° spatial resolution, has been introduced
 222 (see details in Zhang et al., 2020, Fig.S2). With this upscaling scheme, the erosion-induced sediment and
 223 POC delivery from upland soils to the river network, as well as the changes in SOC profiles due to soil
 224 erosion had already been implemented in ORCHIDEE-MUSLE (Zhang et al., 2020). The sediment
 225 delivery from small headwater basins (which are basins without perennial stream and are extracted from
 226 high-resolution (e.g. 3") digital elevation model (DEM) data, Figs. S2a&d) to the river network (i.e. gross
 227 upland soil erosion – sediment deposition within headwater basins) is simulated using the Modified
 228 Universal Soil Loss Equation model (MUSLE, Williams, 1975). As introduced in Zhang et al. (2020),
 229 “the daily sediment delivery rate from each headwater basin (S_{i_ref} , Mg day⁻¹ basin⁻¹) is first calculated for
 230 a given set of reference runoff and vegetation cover conditions (Fig. S2e):

$$231 \quad S_{i_ref} = a(Q_{i_ref} q_{i_ref})^b K_i L S_i C_{ref} P_{ref} \quad (1)$$

232 where Q_{i_ref} is the total water discharge (m³ day⁻¹) at the outlet of headwater basin i for the daily
 233 reference runoff condition (R_{ref}) of 10 mm day⁻¹ (see Table S1 for the definitions of all
 234 abbreviations used in this study). In Eq. 1, q_{i_ref} is the daily peak flow rate (m³ s⁻¹) at the
 235 headwater basin outlet under the assumed reference runoff condition. Similar to the SWAT
 236 model (Soil and Water Assessment Tool, Neitsch et al., 2011), q_{i_ref} was calculated from the
 237 reference maximum 30-minutes runoff (= 1 mm 30-minutes⁻¹) depth and drainage area (DA_i , m²)
 238 according to the following equation:

$$239 \quad q_{i_ref} = \frac{R_{30_ref}}{30 \times 60} (DA_i^{(d DA_i^c)}) 1000 \quad (2)$$

240 where R_{30_ref} (= 1 mm 30-minutes⁻¹) is the assumed daily maximum 30-minutes runoff”. The
 241 coefficients a and b in Eq. 1 and c and d in Eq. 2 need to be calibrated (see section 2.3 and Table
 242 2). In Eq. 1, the term LS_i is the combined dimensionless slope length and steepness factor
 243 calculated based on the DA_i and the average slope steepness (extracted from DEM) of headwater
 244 basin i (Moore and Wilson, 1992). C_{ref} (0-1, dimensionless) in Eq. 1 represents the cover
 245 management factor and is set to 0.1 for the reference state. The soil erodibility factor K_i (Mg MJ
 246 ¹ mm⁻¹) is calculated using the method of the EPIC model (Sharpley and Williams, 1990) based
 247 on SOC and soil texture data obtained from the GSDE database (Table 1). The term P_{ref} (0-1,
 248 dimensionless) in Eq. 1 is a factor representing erosion control practices. It was set to 1, as we

249 did not consider the impacts of soil conservation practices in reducing soil erosion rate. Note that
 250 it does not matter which value is chosen for the R_{ref} , R_{30_ref} and C_{ref} as long as they are used
 251 consistently throughout a study.

252 For the use of these reference sediment delivery estimates in ORCHIDEE- $C_{lateral}$, the values were
 253 first calculated for each headwater basin derived from high resolution geodata (Fig. S2e), then
 254 aggregated to 0.5° grid cells (Fig. S2f) – the scale used in our simulations and required to
 255 maintain computational efficiency (also limited by the availability of climate and land cover
 256 forcing data).

257 This aggregated dataset is then used to force the simulation of the actual daily sediment delivery
 258 (S_j , $\text{g day}^{-1} \text{ grid}^{-1}$) in ORCHIDEE- $C_{lateral}$, simply based on the estimated reference sediment
 259 delivery rates of Eq. (1) and on the ratios between actual runoff and land cover conditions and
 260 the assumed reference conditions used to create that forcing file (Eq. 4, Fig. S2g).

$$261 \quad S_{ref} = \sum_{i=1}^n (S_{i_ref}) \times 10^6 \quad (3)$$

$$262 \quad S_j = S_{ref} \left(\frac{R_j R_{30_j}}{R_{ref} R_{30_ref}} \right)^b \frac{C_j}{C_{ref}} \quad (4)$$

263 where R_j (mm day^{-1}) is the total surface runoff on day j simulated by the hydrological module or
 264 ORCHIDEE-MUSLE at 0.5° spatial resolution every 30 minutes. R_{30_j} (mm 30-min^{-1}) is the
 265 maximum value of the 48 half-hour runoffs in each day. C_j (0-1, unitless) is the daily actual
 266 cover management factor, calculated based on the fraction of surface vegetation cover, the
 267 amount of litter carbon and the biomass of living roots in each PFT within each $0.5^\circ \times 0.5^\circ$ grid
 268 cell. R_{ref} , R_{30_ref} , C_{ref} and P_{ref} are the reference values used to estimate the reference sediment
 269 delivery rates as describe above.

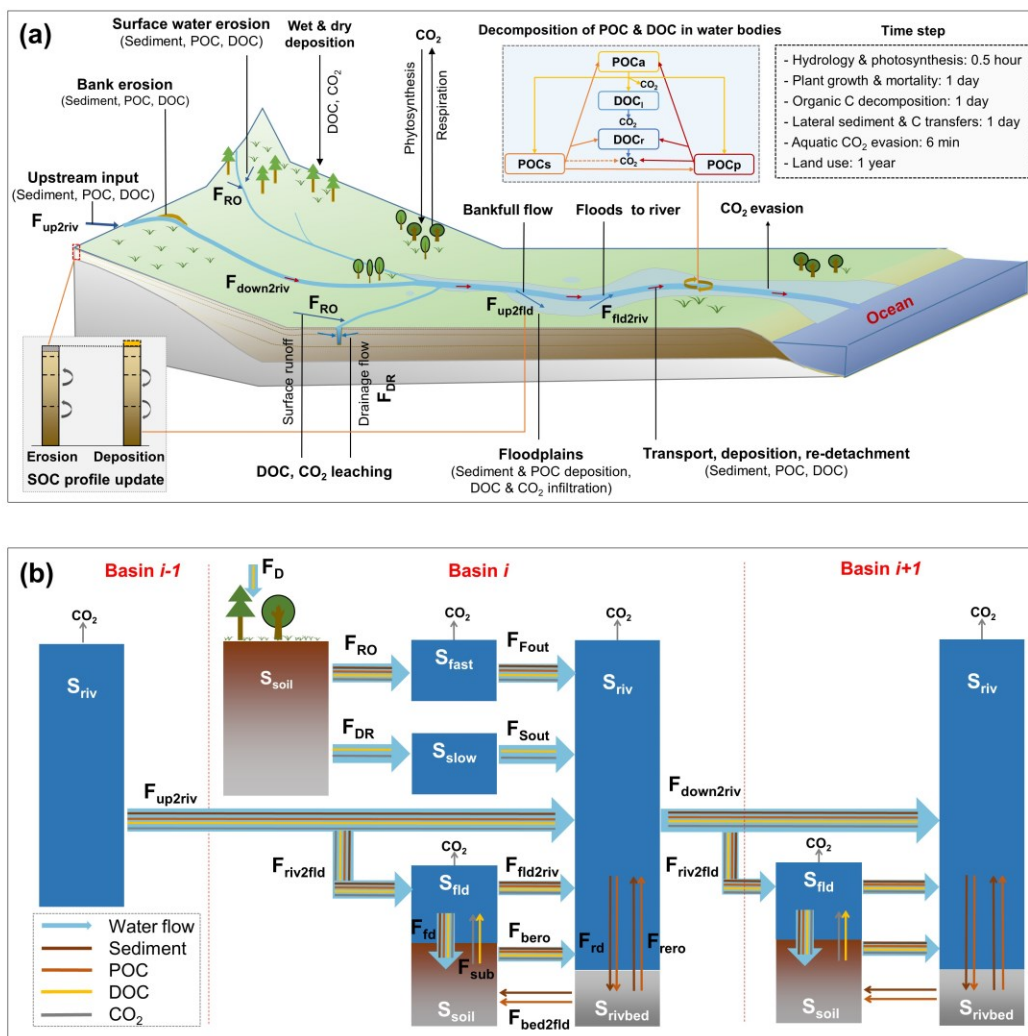
270 Daily POC delivery to river headstream in each 0.5° grid cell is finally simulated based on the
 271 sediment delivery rate and the average SOC concentration of surface soil layers (0-20 cm). The
 272 vertical SOC profile is updated every day based on the average depth of eroded soil for each PFT
 273 in each 0.5° grid cell of ORCHIDEE. For more detailed description of the ORCHIDEE-MUSLE,
 274 we refer to Zhang et al. (2020).

275

276 **2.2 Sediment and POC transport in inland water network**

277 Through the merge of the model branches ORCHILEAK and ORCHIDEE-MUSLE, the new
 278 branch ORCHIDEE-C_{lateral} combines the novel features of both sources (DOC and POC)
 279 described above. The development of ORCHIDEE-C_{lateral} is complemented by a representation of
 280 the sediment and POC transport through the river network that is completely novel and described
 281 below.

282 **2.2.1 Sediment transport**



283
 284 **Figure 1** Simulated lateral transfer processes of water, sediment and carbon (POC, DOC and
 285 CO₂) in ORCHIDEE-C_{lateral} (a) and a schematic plot for the reservoirs and flows of water,
 286 sediment and carbon represented in the routing module of ORCHIDEE-C_{lateral} (b). S_{soil} is the soil

287 pool. S_{rivbed} is the sediment (also POC) deposited on the river bed. S_{fast} , S_{slow} , S_{riv} and S_{fld} are the
 288 ‘fast’, ‘slow’, stream and flooding water reservoir, respectively. F_{RO} and F_{DR} are the surface
 289 runoff and belowground drainage, respectively. F_{Fout} and F_{Sout} are the flows from fast and slow
 290 reservoir to the stream reservoir, respectively. F_{up2riv} and $F_{down2riv}$ are the upstream inputs and
 291 downstream outputs, respectively. $F_{riv2fld}$ is the outputs from river stream to the flooding
 292 reservoir. $F_{fld2riv}$ is the return flow from flooding reservoir to stream reservoir. $F_{bed2fld}$ is the
 293 transform from deposited sediment in river bed to floodplain soil. F_{bero} is bank erosion. F_{rd} and
 294 F_{rero} are the deposition and re-detachment of sediment and POC in river channel, respectively.
 295 F_{sub} is the flux of DOC and CO_2 from floodplain soil (originated from the decomposition of
 296 submerged litter and soil carbon) to the overlying flooding water. F_{fd} is the deposition of
 297 sediment and POC and the infiltration of water and DOC. F_D is the wet and dry deposition of
 298 DOC from atmosphere and plant canopy. DOC_1 and DOC_r are the labile and refractory DOC
 299 pool, respectively. POC_a , POC_s and POC_p are the active, slow and passive POC pool,
 300 respectively.

301 Simulation of sediment transport through the river network basically follows the routing scheme
 302 of surface water and DOC of ORCHILEAK (Fig. 1). Along with surface runoff (F_{RO_h2o} , $m^3 \text{ day}^{-1}$),
 303 the sediment delivery (F_{RO_sed} , $g \text{ day}^{-1}$) from uplands in each basin (i.e. each 0.5° grid cell in
 304 the case of this study) initially feeds an aboveground water reservoir (S_{fast_h2o} , m^3) with a so-
 305 called fast water residence time. From this fast water reservoir, a delayed outflow feeds into the
 306 so-called stream reservoir (S_{riv} , m^3 , Fig. 1b). Daily water (F_{Fout_h2o} , $m^3 \text{ day}^{-1}$) and sediment
 307 (F_{Fout_sed} , $g \text{ day}^{-1}$) flows from fast water reservoir to stream reservoir are calculated from a grid
 308 cell-specific topographic index f_{topo} (unitless, Vörösmarty et al., 2000) extracted from a forcing
 309 file (Table 1) and a reservoir-specific factor τ which translates f_{topo} into a water residence time of
 310 each reservoir (Eqs. 5, 6). Following Guimberteau et al. (2012), the τ of the fast water reservoir
 311 (τ_{fast}) is set to 3.0 days. As the sediment delivery calculated from MUSLE is the net soil loss
 312 from headwater basins (gross soil erosion – soil deposition within headwater basins), we
 313 assumed that there is no sediment deposition in the fast reservoir, and that all of the sediment in
 314 the fast reservoir enters the stream reservoir. In addition, only the surface runoff causes soil
 315 erosion. The belowground drainage (F_{DR_h2o} , $m^3 \text{ day}^{-1}$) only transports DOC and dissolved CO_2
 316 to the stream reservoir (Fig. 1b).

317
$$F_{Fout_h2o} = \frac{S_{fast_h2o}}{\tau_{fast} f_{topo}} \quad (5)$$

318
$$F_{Fout_sed} = \frac{S_{fast_sed}}{\tau_{fast} f_{topo}} \quad (6)$$

319 The budget of the suspended sediment in the stream (S_{riv_sed} , g) is determined by F_{out_sed} , the
 320 upstream sediment input (F_{up2riv_sed} , g day⁻¹), the sediment input by flooding water returning to
 321 the river ($F_{fld2riv_sed}$, g day⁻¹), the re-detachment of the previously deposited sediment in the river
 322 bed (F_{rero_sed} , g day⁻¹), the bank erosion (F_{bero_sed} , g day⁻¹), the sediment deposition in the river
 323 bed (F_{rd_sed} , g day⁻¹) and the sediment transported to downstream river stretches ($F_{down2riv_sed}$, g
 324 day⁻¹) and, occasionally, floodplains ($F_{riv2fld_sed}$, g day⁻¹) (Eq. 7).

325
$$\frac{dS_{riv_sed}}{dt} = F_{Fout_sed} + F_{up2riv_sed} + F_{fld2riv_sed} + F_{rero_sed} + F_{bero_sed} - F_{rd_sed} - F_{down2riv_sed} - F_{riv2fld_sed} \quad (7)$$

326 Sediment transport capacity (TC , g m⁻³), defined as the maximum load of sediment that a given
 327 flow rate can carry, determines the amount of suspended sediment that can be transported to the
 328 downstream grid cell (e.g. $F_{down2riv_sed}$, $F_{riv2fld_sed}$), as well as the amount of suspended sediment
 329 that will deposit on the river bed (F_{rd_sed}) or the erosion rate of the river bed (F_{rero_sed}) or river
 330 bank (F_{bero_sed}) (Arnold et al., 1995; Nearing et al., 1989; Neitsch et al., 2011).

331 In this study, we used an empirical equation adapted from the WBMsed model, which has been
 332 proven effective in simulating the suspended sediment discharges in global large rivers (Cohen et
 333 al., 2014), to estimate the TC (g m⁻³) of stream flow:

334
$$TC = \frac{\omega q_{ave}^{0.3} A^{0.5} \left(\frac{q_{iday}}{q_{ave}}\right)^{e_1} (24 \times 60 \times 60)}{F_{down2riv_h2o}} \quad (8)$$

335
$$e_1 = 1.5 - \max(0.8, 0.145 \log_{10} DA) \quad (9)$$

336 where ω is the coefficient of proportionality, q_{ave} (m³ s⁻¹) is long-term average stream flow rate
 337 obtained from an historical simulation by ORCHILEAK (Table 1), q_j (m³ s⁻¹) is stream flow rate
 338 on day j , e_1 is an exponent depending on the upstream drainage area (DA , m²), $F_{down2riv_h2o}$ (m³
 339 day⁻¹) is the daily downstream water discharge from the stream reservoir. In the stream reservoir
 340 of each basin, net deposition occurs when TC is smaller than the concentration of suspended
 341 sediment, and the daily deposited sediment (F_{rd_sed} , g day⁻¹) is calculated based on the surplus of
 342 the suspended sediment:

$$343 \quad F_{rd_sed} = c_{rivdep}(S_{riv_sed} - TC S_{riv_h2o}) \quad (10)$$

344 where c_{rivdep} (0-1, unitless) is the daily deposited fraction of the sediment surplus. Net erosion of
 345 the previously deposited sediment in river bed (S_{rivbed_sed} , Fig. 1) or the river bank occurs when
 346 TC is larger than the concentration of suspended sediment. We assumed that the erosion of river
 347 bank occurs only after all of the S_{rivbed_sed} has been eroded. Thus the daily erosion rate (F_{rero_sed} , g
 348 day⁻¹) in river channel is calculated as:

$$349 \quad F_{rero_sed} = \begin{cases} c_{ebed}(TC S_{riv_h2o} - S_{riv_sed}), & c_{ebed}(TC S_{riv_h2o} - S_{riv_sed}) \leq S_{rivbed_sed} \\ S_{rivbed_sed} + c_{ebank}(TC S_{riv_h2o} - S_{riv_sed} - S_{rivbed_sed}), & c_{ebed}(TC S_{riv_h2o} - S_{riv_sed}) > S_{rivbed_sed} \end{cases} \quad (11)$$

350 where c_{ebed} (0-1, unitless) and c_{ebank} (0-1, unitless) are the fraction of sediment deficit that can be
 351 complemented by erosion of river bed and bank, respectively. After updating the S_{riv_sed} based on
 352 the F_{rd_sed} or F_{rero_sed} , the sediment discharge to downstream basin ($F_{down2riv_sed}$, g day⁻¹) is
 353 calculated based on the ratio of downstream water discharge to the total stream reservoir:

$$354 \quad F_{down2riv_sed} = (S_{riv_sed} - F_{rd_sed} + F_{rero_sed}) \frac{F_{down2riv_h2o}}{S_{riv_sh2o}} \quad (12)$$

355 In each basin, the bankfull flow occurs when S_{riv_h2o} exceeds the maximum water storage of river
 356 channel (S_{rivmax} , g), which is defined by a forcing file (Table 1). Sediment flow from stream to
 357 floodplain ($F_{riv2fld_sed}$, g day⁻¹) follows the flooding water, and it is calculated as:

$$358 \quad F_{riv2fld_sed} = (S_{riv_sed} - F_{rd_sed} + F_{rero_sed}) \frac{F_{riv2fld_h2o}}{S_{riv_sh2o}} \quad (13)$$

$$359 \quad F_{riv2fld_h2o} = (S_{riv_h2o} - F_{down2riv_h2o} - S_{rivmax}) \frac{f_{A_fld}}{f_{A_fld} + f_{A_riv}} \quad (14)$$

360 where f_{A_fld} (0-1, unitless) and f_{A_riv} (0-1, unitless) is the fraction of floodplain area and river
 361 surface area in each basin, respectively. Following the routing scheme of ORCHILEAK, the
 362 bankfull flow of a specific basin is assumed to enter the floodplain in the neighbouring
 363 downstream basin instead of the basin where it originates.

364 The sediment balance in flooding reservoir (S_{fld_sed} , g) is controlled by sediment input from the
 365 upstream basins ($F_{riv2fld_sed}$, g day⁻¹), the sediment flowing back to the stream reservoir ($F_{fld2riv_sed}$,
 366 g day⁻¹) and the sediment deposition (F_{fd_sed} , g day⁻¹) (Fig. 1):

$$367 \quad \frac{dS_{fld_sed}}{dt} = F_{riv2fld_sed} - F_{fld2riv_sed} - F_{fd_sed} \quad (15)$$

368 Sediment deposition in floodplain is calculated as the sum of a natural deposition and the
 369 deposition due to evaporation (E_{h2o} , $m^3 \text{ day}^{-1}$) and infiltration (I_{h2o} , $m^3 \text{ day}^{-1}$) of the flooding
 370 waters:

$$371 \quad F_{fld_sed} = c_{flddep} S_{fld_sed} + S_{fld_sed} \frac{E_{h2o} + I_{h2o}}{S_{fld_h2o}} \quad (16)$$

372 where c_{flddep} (0-1, unitless) is the daily deposited fraction of the suspended sediment in flooding
 373 waters. After removing the deposited sediment from S_{fld_sed} , $F_{fld2riv_sed}$ is calculated based on the
 374 ratio of ratio of $F_{fld2riv_h2o}$ to the total flooding reservoir:

$$375 \quad F_{fld2riv_sed} = S_{fld_sed} \frac{F_{fld2riv_h2o}}{S_{fld_h2o} - E_{h2o} - I_{h2o}} \quad (17)$$

376

$$377 \quad F_{fld2riv_h2o} = \frac{S_{fld_h2o} - E_{h2o} - I_{h2o}}{\tau_{flood} f_{topo}} \quad (18)$$

378 where τ_{flood} is a factor which translates f_{topo} (Table 1) into a water residence time of the flooding
 379 reservoir. Same to ORCHILEAK, it is set to 1.4 (day m^{-2}) in this study.

380 Note that as the upland soil in ORCHIDEE is composed of clay, silt and sand particles, so that
 381 the dynamics of clay-, silt- and sand-sediment in inland waters are simulated separately. To
 382 represent the selective transport of clay-, silt- and sand-sediment, the model parameter ω (Eq. 8)
 383 and c_{rivdep} (Eq. 10) are set to different values when calculating the sediment transport capacity
 384 and the deposition of surplus suspended sediment for different particle sizes (Table 2).

385 Moreover, as our model mainly aims to simulate the lateral transfer of sediment and carbon at
 386 the decadal to centennial timescale, rather than covering the past thousands of years or even
 387 longer time periods, we did not consider the evolution and diversion of river channels in our
 388 study.

389 **2.2.2 POC transport and decomposition**

390 Many studies described the selective transport of POC and sediment of different particle sizes.
 391 The enrichment ratio (defined as the ratios of fraction of any given component in the transported
 392 sediment to that in the eroded soils) of POC in the transported sediment generally showed
 393 significant positive correlation to the fine sediment particles (e.g. fine silt and clay), but negative

394 correlation to the coarse sediment particles (Galy et al., 2008; Haregeweyn et al., 2008; Nadeu et
395 al., 2011; Nie et al., 2015). In ORCHIDEE-C_{lateral}, the physical movements of POC in inland
396 water systems are simply assumed to follow the flows of finest clay-sediment (Fig. 1b). For
397 example, the fractions of riverine suspended POC which is deposited on the river bed (F_{rd_POC} , g
398 C day⁻¹) or is transported to the river channel ($F_{down2riv_POC}$, g C day⁻¹) or floodplain ($F_{riv2fld_POC}$,
399 g C day⁻¹) are assumed to be equal to the corresponding fractions of clay-sediment (Eqs. 19-21).
400 Also flows of suspended POC in flooding waters to floodplain soil (F_{fd_POC} , g C day⁻¹) or back to
401 the stream reservoir ($F_{fld2riv_POC}$, g C day⁻¹), as well as the resuspension of POC from the river
402 bed (F_{rero_POC} , g C day⁻¹) are scaled to the simulated flows of clay-sediment (Eqs. 22-24). Note
403 that, similar to SOC, the POC in aquatic reservoirs are divided into three pools: the active
404 (POC_a), slow (POC_s) and passive pool (POC_p) (Fig. 1a). The eroded active, slow and passive
405 SOC flow into the corresponding POC pools in the ‘fast’ water reservoir (Fig. 1b).

$$406 \quad F_{rd_POC} = S_{riv_POC} \frac{F_{rd_sed_clay}}{S_{riv_sed_clay}} \quad (19)$$

$$407 \quad F_{down2riv_POC} = S_{riv_POC} \frac{F_{down2riv_sed_clay}}{S_{riv_sed_clay}} \quad (20)$$

$$408 \quad F_{riv2fld_POC} = S_{riv_POC} \frac{F_{riv2fld_sed_clay}}{S_{riv_sed_clay}} \quad (21)$$

$$409 \quad F_{fd_POC} = S_{fld_POC} \frac{F_{fd_sed_clay}}{S_{fld_sed_clay}} \quad (22)$$

$$410 \quad F_{fld2riv_POC} = S_{fld_POC} \frac{F_{fld2riv_sed_clay}}{S_{fld_sed_clay}} \quad (23)$$

$$411 \quad F_{bed2fld_POC} = S_{rivbed_POC} \frac{F_{bed2fld_sed}}{S_{rivbed_sed}} \quad (24)$$

412 The representation of POC dynamics in the aquatic reservoirs and bed sediment involve as well
413 decomposition, which follows largely the scheme used for SOC (Fig. 1a). However, instead of
414 using the rate modifiers for soil temperature and moisture used in the soil carbon module, daily
415 decomposition rates (F_{POC_i} , g C day⁻¹) of each POC pool (S_{POC_i} , g C) are simulated to vary with
416 water temperature based on the Arrhenius term which is used to simulate the DOC
417 decomposition in ORCHILEAK (Hanson et al., 2011; Lauerwald et al., 2017):

$$F_{POC_i} = S_{POC_i} \frac{1.073^{(T_{water}-28.0)}}{\tau_{poc_i}} \quad (25)$$

419 where T_{water} (°C) is the temperature of water reservoirs and is calculated from local soil
 420 temperature using an empirical function (Lauerwald et al., 2017). For the POC stored in bed
 421 sediment, temperature of the stream reservoir is used to calculate the decomposition rate. τ_{POC_i} is
 422 the turnover time of the i (active, slow and passive) POC pool. We assumed that the base
 423 turnover times of active (0.3 year) and slow (1.12 years) POC pools are the same as for the
 424 corresponding SOC pools. The passive SOC pool is generally regarded as the SOC which is
 425 associated to soil minerals or enclosed in soil aggregates (Parton et al., 1987). During the soil
 426 erosion and sediment transport processes, the aggregates break down and the passive POC loses
 427 its physical protection from decomposition (Chaplot et al., 2005; Hu and Kuhn, 2016; Polyakov
 428 and Lal, 2008; Wang et al., 2014a). To represent the acceleration of passive POC decomposition
 429 due to aggregate breakdown, we assume that the turnover time of the passive POC is same to the
 430 active POC (0.3 year), rather than the passive SOC (462 years). Similar to the scheme used to
 431 simulate SOC decomposition in ORCHILEAK, the decomposed POC from each of the active,
 432 slow and passive pool flows to other POC pools, to DOC pools or is released to the atmosphere
 433 as CO₂ (Fig. 1). Fractions of the decomposed POC flowing to different POC and DOC pools or
 434 to the atmosphere are set to the same values used in ORCHILEAK for simulating the fates of the
 435 decomposed SOC pools.

436 Changes in the vertical SOC profile of floodplain soils following sediment deposition is
 437 simulated at the end of every daily modelling time-step, after physical transfers and
 438 decomposition of POC have been calculated. The sediment deposited on the floodplain becomes
 439 part of the surface soil layer, and the active, slow and passive POC flow into the active, slow and
 440 passive SOC pools in surface soil layer, respectively. SOC in the original surface and subsurface
 441 soil layers is transferred sequentially to the adjacent deeper soil layers. As the vertical soil profile
 442 in ORCHILEAK is described by an 11-layer discretization of a 2 m soil column, we introduce a
 443 deep (> 2 m) soil pool (S_{deep}) to represent the soil and carbon transferred down from the 11th soil
 444 layer following ongoing floodplain deposition. Decomposition rates of the organic carbon in this
 445 deep soil pool are assumed to be same to those in the 11th (deepest) soil layer. Note that when
 446 the soil erosion rate of the floodplain soil is larger than the sediment deposition rate, sediment
 447 and organic carbon in S_{deep} move up to replenish the stocks of the 11th soil layer.

448 2.3 Model application and evaluation

449 In this study, ORCHIDEE-C_{lateral} was applied over Europe and parts of Middle East (-30W– 70E,
450 34N-75N, Fig. S4), where extensive observation datasets are available to calibrate and evaluate
451 our model (Table 1). The return period of daily bankfull flow ($P_{flooding}$, year), which represents
452 the average interval between two flooding events and is used in this study to produce the forcing
453 file of S_{rivmax} from a pre-run of ORCHILEAK. Note that $P_{flooding}$ is generally shorter than the
454 return period of real flooding events, as the flooding may occur in several continuous days and
455 all the flooding waters occurring on these continuous days are generally regarded to belong to
456 the same flooding event (supplementary Fig. S3). To our knowledge, existing observational data
457 on $P_{flooding}$ are still very limited. Therefore, following Schneider *et al.* (2011), we also use a
458 constant $P_{flooding}$ to simulate the bankfull flows from European rivers and the observed long-term
459 (1961–2000) average bank full flow rate ($\text{m}^3 \text{s}^{-1}$) at 66 sites obtained from Schneider *et al.* (2011)
460 was used to calibrate $P_{flooding}$ (the optimized value is 0.1 year, Table 2). Following Zhang *et al.*
461 (2020), the parameters a , b , c and d in Eq. 1 and 2 (Table 2) were calibrated at 57 European
462 catchments (Fig. S4d) against the modelled sediment delivery data obtained from the European
463 Soil Data Centre (ESDAC, Borrelli *et al.*, 2018). The sediment delivery data from the ESDAC
464 product is simulated by the WaTEM/SEDEM model using high-resolution data of topography,
465 soil erodibility, land cover and rainfall. It has been calibrated and validated using observed
466 sediment fluxes from 24 European catchments (Borrelli *et al.*, 2018).

467 Parameters controlling sediment transport, deposition and re-detachment (i.e. ω , C_{rivdep} , C_{flddep} ,
468 C_{ebed} and C_{ebank} , Table 2) in stream and flooding reservoirs were calibrated against the observed
469 long-term averaged sediment discharge rate (Table 1). We also conducted a sensitivity analysis
470 to test the sensitivity of the simulated riverine sediment and carbon discharges to these
471 parameters, following the method used in Tian *et al.* (2015). The sensitivity of simulation results
472 was evaluated based on the relative changes in simulated riverine sediment and carbon
473 discharges to a 10% increase and decrease of each parameter (Table 2). Result of the sensitivity
474 analysis shows that the simulated riverine sediment and POC discharges are most sensitive to
475 C_{rivdep} in Eq. 10, followed by ω in Eq. 8 (Fig. S5). Compared to C_{rivdep} and ω , the simulated
476 riverine sediment and POC discharges are less sensitive to C_{flddep} , C_{ebed} and C_{ebank} . With 10%
477 changes in C_{flddep} , C_{ebed} or C_{ebank} , the changes in riverine sediment and POC discharges are

478 generally less than 3%. In addition, the changes in simulated riverine DOC and CO₂ discharges
 479 are mostly less than 1% with 10% changes in ω , C_{flddep} , C_{ebed} and C_{ebank} . Nonetheless, a 10%
 480 change in C_{rivdep} can lead to a change of about 5% in the simulated riverine CO₂ discharge (Fig.
 481 S5).

482 **Table 2** Values of the key parameters used in the ORCHIDEE-C_{lateral} to simulate the lateral
 483 transfer of sediment and carbon.

Parameter	Value	Unit	Description	Source
a	26.96	Unitless	Coefficient in Eq. 1	Calibrated
b	0.76	Unitless	Coefficient in Eq. 1	Calibrated
c	1.79	Unitless	Coefficient in Eq. 2	Calibrated
d	-0.065	Unitless	Coefficient in Eq. 2	Calibrated
C_{ebed}	0.5	Unitless (0-1)	The fraction of sediment deficit that can be complemented by erosion of river bed (Eq. 6)	Calibrated
C_{ebank}	0.5	Unitless (0-1)	The fraction of sediment deficit that can be complemented by erosion of river bank (Eq. 6)	Calibrated
C_{rivdep}	0.1, 0.2, 0.5 ^a	Unitless (0-1)	Daily deposited fraction of the sediment surplus in stream reservoir (Eq. 5)	Calibrated
C_{flddep}	0.5, 1.0, 1.0 ^a	Unitless (0-1)	Daily deposited fraction of the sediment surplus in flooding reservoir (Eq. 11)	Calibrated
$P_{flooding}$	0.1	year	Return period of daily bankfull flow	Calibrated
τ_{fast}	3.0	day	A factor which translates the topographic index into the water residence time of the 'fast' reservoir (Eqs. 5, 6)	Guimberteau et al., 2012
τ_{flood}	1.4	day	A factor which translates the topographic index into the water residence time of the flooding reservoir (Eq. 18)	Guimberteau et al., 2012
τ_{poc}	0.3, 1.12, 0.3 ^b	year	A factor which translates the topographic index into the water residence time of the flooding reservoir (Eq. 25)	Lauerwald et al., 2017
ω	12.0, 5.0, 2.5 ^a	g s ⁻¹	Coefficient of proportionality for calculating sediment transport capacity (Eq. 8)	Calibrated

484 ^a For clay, silt and sand sediment, respectively. ^b For active, slow and passive POC, respectively.

485

486 After parameter calibration, ORCHIDEE-C_{lateral} was applied to simulate the lateral transfers of
487 water, sediment and organic carbon in European rivers over the period 1901-2014. Before this
488 historical simulation, ORCHIDEE-C_{lateral} was run over 10,000 years (spin-up) until the soil
489 carbon pools reached a steady state. In the ‘spin-up’ simulation, the PFT maps, atmospheric CO₂
490 concentrations and meteorological data during 1901–1910 were used repeatedly as forcing data.
491 The finally simulated water discharge rates in European rivers were evaluated using observation
492 data at 93 gauging sites (locations see Fig. S4a) from the Global Runoff Data Base (GRDC,
493 Table 1). The simulated bankfull flows were evaluated against observed long-term (1961–2000)
494 average bankfull flows at 66 sites (Fig. S4b) from Schneider *et al.* (2011). The simulated riverine
495 sediment discharge rate is evaluated using observation data from the European Environment
496 Agency and existing publications (see Table 1) at 221 gauging sites (Fig. S4c). The riverine total
497 organic carbon (TOC), POC and DOC concentrations provided by the GLObal RIver Chemistry
498 Database (GLORICH, Hartmann *et al.*, 2019) at 346 sites (Fig. S4d) were used to evaluate the
499 simulated riverine POC and DOC concentrations. Note that observations in the GLORICH
500 database which are measured at gauging sites with drainage area $<1.0 \times 10^4$ km² were excluded
501 from our model evaluation, because these small catchments cannot be represented by the coarse
502 river network scheme at 0.5 degree (ca. 55 km at the equator). Among the retained 346 gauging
503 sites, TOC concentrations were measured at 188 sites, DOC was measured at 314 sites. POC was
504 measured at only two sites (Bad honnef (51 measurements) and Bimmen (78 measurements)) in
505 the Rhine catchment and one site (Rheine, 36 measurements) in the Ems catchment (Fig. S4d).

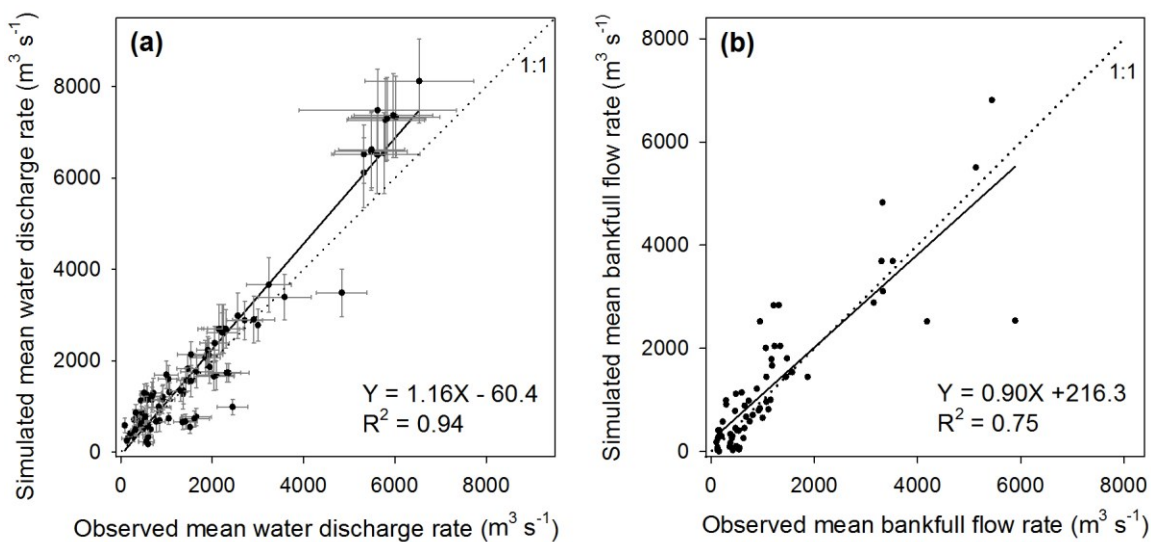
506 **3 Results and Discussion**

507 **3.1 Model evaluation**

508 **3.1.1 Stream water discharge and bankfull flow**

509 Evaluation of our simulation results using *in situ* observation data from Europe rivers indicates
510 that ORCHIDEE-C_{lateral} well reproduces the magnitude and interannual variation of water
511 discharge rates in major European rivers (Figs. 2a and S6). Overall, the simulated riverine water
512 discharge rate explained 94% (Fig. 2a) of the spatial variation of the observed long-term average
513 water discharge rates across 93 gauging sites in Europe (Fig. S4a). Relative biases (calculated as:
514 $\frac{\text{simulation} - \text{observation}}{\text{observation}} \times 100\%$, as used through the manuscript if not otherwise stated) of the

515 simulated average water discharge rates compared to the observations are mostly smaller than
 516 30% (Fig. 2a). For major European rivers, such as the Rhine, Danube, Elbe, Rhone and Volga,
 517 ORCHIDEE-C_{lateral} also captures the interannual variation of the water discharge rate (Fig. S6).
 518 We recognize that ORCHIDEE-C_{lateral} may overestimate or underestimate the water discharge
 519 rate in some rivers (Fig. 2a), particularly in smaller rivers where discrepancy between the stream
 520 routing scheme (delineation of catchment boundaries) extracted from the forcing data at 0.5°
 521 resolution and the real river network (Fig. S7) can be substantial. An over-estimation or
 522 underestimation of the catchment area by the forcing data as respectively found for the Elbe and
 523 Rhine will introduce a proportional bias in the average amount of simulated discharge from these
 524 catchment. Another problem are stream channel bifurcations which occur in reality, but which
 525 are not represented in a stream network derived from a digital elevation model. For example, in
 526 the Danube river delta, a fraction of the discharge is actually exported to the sea through the
 527 Saint George Branch, in addition to the water discharge through the main river channel (Fig.
 528 S7b). This explains why the simulated water discharge rate at the outlet of the Danube catchment
 529 is larger than the observation at the Ceatal gauging station, Romania (identify number in the
 530 GRDC database is 6742900, Fig. S6m), where only the main stream discharge was measured.



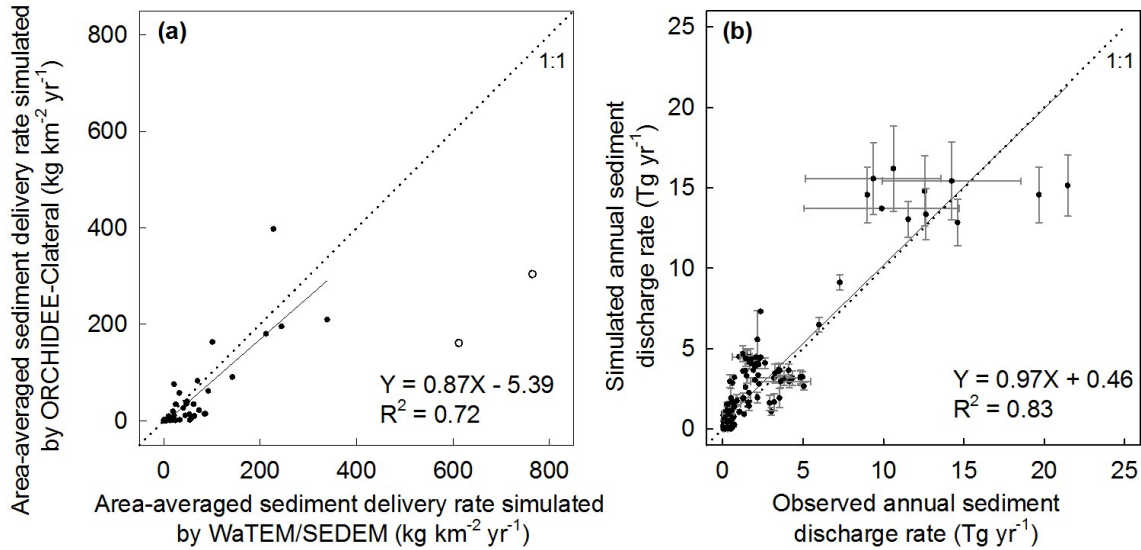
531
 532 **Figure 2** Comparison between observed and simulated riverine water discharge rates (a) and
 533 bankfull flow rates (b). In figure (a), the error bar denotes the standard deviation of interannual
 534 variation. Sources of the observed riverine water discharge rate and bankfull flow rate can be
 535 found in Table 1.

536 With the calibrated return period (= 0.1 year) of the daily flooding rate (see section 2.3), the
537 simulated bankfull flow rates compare well to observations at the 66 sites for which data was
538 available (Fig. 2b). Overall, the simulation result explained 75% of the inter-site variation of the
539 observed bankfull flow rates. Relative biases of the simulated bankfull flow rates are generally
540 lower than 30%, although the relative bias may be larger than 100% at some sites.

541 **3.1.2 Sediment transport**

542 The simulated area-averaged sediment delivery rates from upland to river network by the
543 ORCHIDEE- $C_{lateral}$ are overall comparable to those simulated by the WaTEM/SEDEM for most
544 catchments in Europe (Figs. 3a and S4d). In the two catchments in the Apennine Peninsula,
545 ORCHIDEE- $C_{lateral}$ gives a drastically lower estimation on the sediment delivery rates compared
546 to WaTEM/SEDEM. By excluding these two catchments, ORCHIDEE- $C_{lateral}$ reproduces 72% of
547 the spatial variation of the sediment delivery rates estimated by the WaTEM/SEDEM (Fig. 3a).
548 In addition, the average sediment loss rate over all catchments showed in Fig. S4d is 40.8 g m^{-2}
549 yr^{-1} , which is overall comparable to the estimate by the WaTEM/SEDEM ($42.5 \text{ g m}^{-2} \text{ yr}^{-1}$).

550 ORCHIDEE- $C_{lateral}$ reproduces 83% of the inter-site variation of the sediment discharge rates
551 across Europe (Fig. 3b). Simulation of the riverine sediment discharge rate at large spatial scale
552 is still a big challenge. It generally needs detailed information on the stream flow, geomorphic
553 properties of river channel and the particle composition of the suspended sediment (Neitsch et
554 al., 2011). Moreover, the parameters of existing sediment transport models usually require
555 recalibration when they are applied to different catchments (Gassman et al., 2014; Oeurng et al.,
556 2011; Vigiak et al., 2017). In ORCHIDEE- $C_{lateral}$, the sediment processes in river networks are
557 simulated using simple empirical functions and parameters based on a routing scheme at a spatial
558 resolution of 0.5° (section 2.2.1). Detailed information about the stream flow (e.g. cross-
559 sectional area) and the geomorphic properties of river channels are not represented. Sediment
560 discharge in all catchments was simulated using a universal parameter set. This may explain why
561 ORCHIDEE- $C_{lateral}$ fails to capture the sediment discharge rates in some specific catchments,
562 especially those with relatively small drainage areas (e.g. $< 5 \times 10^3 \text{ km}^2$).



563

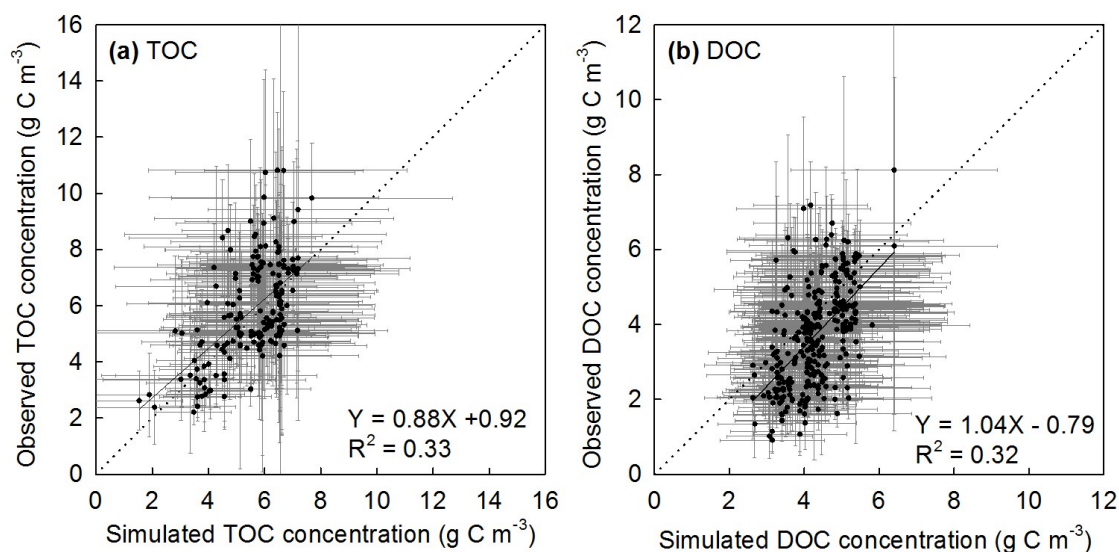
564 **Figure 3** Comparison between the simulated area-averaged sediment delivery rate from uplands
 565 to river network from ORCHIDEE-C_{lateral} and WaTEM/SEDEM (a), and the comparison between
 566 observed and simulated annual sediment discharge rates at 221 gauging sites (b). In figure (a),
 567 the two hollow dots represent the sediment delivery rates at the two catchments in the Apennine
 568 Peninsula (Fig. S4d). The regression function in figure (a) was obtained based on the values of
 569 all solid dots, excluding the two hollow dots. In figure (b), the error bar denotes the standard
 570 deviation of interannual variation. Sources of the observed annual sediment discharge rate in
 571 Table 1.

572 3.1.3 Organic carbon transport

573 Simulation of the riverine carbon discharge rate at large spatial scale is even a bigger challenge
 574 than simulating sediment discharge, as the riverine carbon discharge is controlled by many
 575 factors, such as upland topsoil SOC concentrations, soil erosion rate, transport and deposition
 576 rate of clay fraction in river channel and on floodplain, and the decomposition of POC in transit
 577 and in aquatic sediments. As described above, the simulated water discharge rate, bankfull flow
 578 and sediment discharge rate are overall comparable to observation (Figs. 2 and 3). The simulated
 579 total SOC stock in the top 0-30 cm soil layer in Europe of 107 Pg C is close to the value
 580 extracted from the HWSD database (106 Pg C), but significantly lower than the values extracted
 581 from some other databases, such as the GSDE (249 Pg C), SoilGrids (202 Pg C), S2017 (148 Pg
 582 C) and landGIS (226 Pg C) (Fig. S8a). Distribution of the simulated SOC stock along the latitude
 583 gradients (30° N – 75° N) are overall comparable to those extracted from the HWSD and S2017

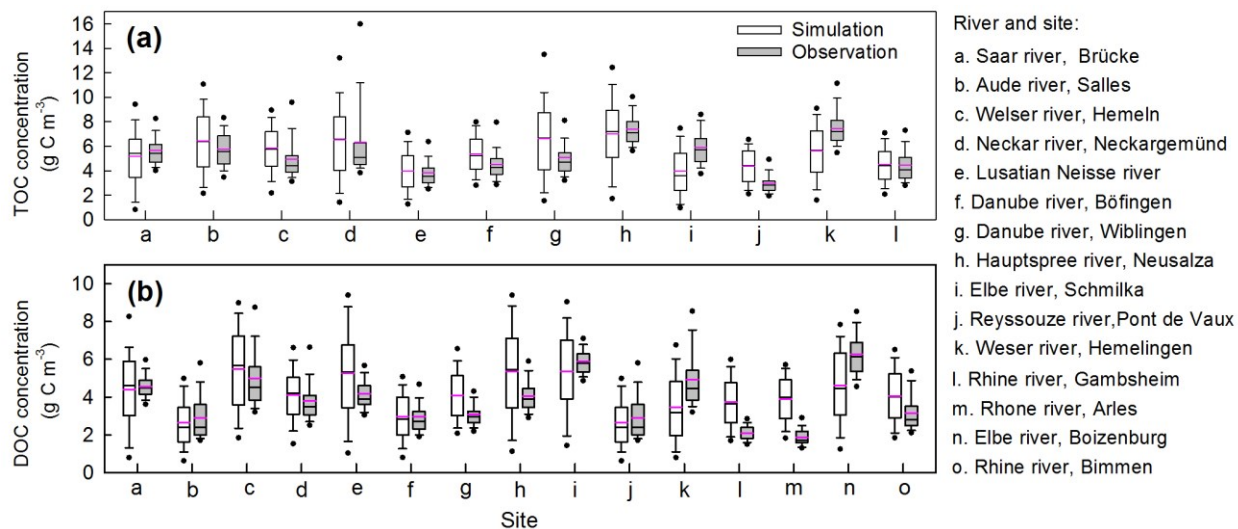
584 databases (Fig. S8). But even compared to these two databases, our model still underestimated
585 the SOC stock in southern Europe (30° N – 41° N).

586 Comparison of the simulated concentrations of riverine organic carbon and the observations
587 obtained from the GLORICH database (Hartmann et al., 2019) indicates that our model can
588 basically capture the TOC and DOC concentrations in European rivers (Figs 4, 5, S9 and S10).
589 The simulation results explain 34% and 32% of the inter-site variation of the observed TOC and
590 DOC concentrations, respectively (Fig. 4). For major European rivers, such as the Rhine, Elbe,
591 Danube, Spree and Weser, the simulated long-term average TOC and DOC concentrations are
592 overall close to the observations (Figs. 5, S9 and S10). But for the Rhone river in southern
593 France, the DOC concentrations have been systematically overestimated by more than 50%
594 (Figs. 5 and S10m). In addition, both simulated and observed TOC and DOC concentrations
595 show drastic temporal (both seasonal and interannual) variations (Figs 4, S9 and S10). Our
596 model seems to have overestimated the temporal variation of TOC and especially DOC
597 concentrations (Figs. S9 and S10). Nonetheless, the simulated temporal variation of TOC and
598 DOC discharge rates are overall comparable to the observation (Figs. S11 and S12), as our
599 model can well capture the magnitude and temporal variation of riverine water discharge rates.



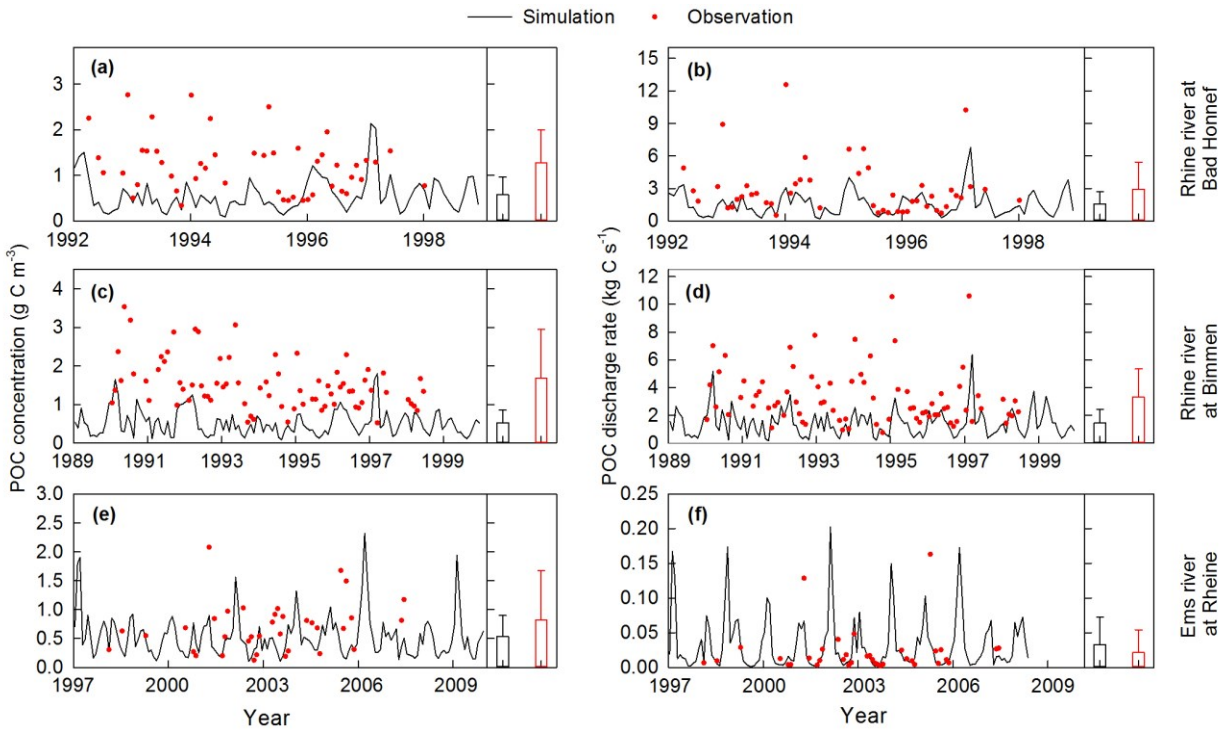
600
601 **Figure 4** Comparison between the observed and simulated riverine TOC (a, POC+DOC) and
602 DOC (b) concentrations. The dot and error bar denote the mean and standard deviation at each
603 gauging site, respectively. Note that the mean and standard deviation of the simulated

604 concentrations at each site are calculated based on the monthly average value, but the mean and
 605 standard deviation of the observed concentrations are based on instantaneous observation.



606
 607 **Figure 5** Comparison between the observed and simulated concentrations of total organic carbon
 608 (TOC, a) and dissolved organic carbon (DOC, b) in river flows. The black and pink lines in each
 609 box denote the median and mean value, respectively. Box boundaries show the 25th and 75th
 610 percentiles, whiskers denote the 10th and 90th percentiles, the dots below and above each box
 611 denote the 5th and 95th percentiles, respectively.

612 In Europe, the GLORICH database only provides POC concentrations measured at three gauging
 613 stations in northwestern Germany (Figs. 6, S4d). The simulated POC concentrations and
 614 discharge rates in the Ems river at Rheine are overall comparable to the observation (Figs. 6e,f).
 615 However, at the two gauging sites at the river Rhine, the POC concentrations have been
 616 significantly underestimated (Figs. 6a-d). We noticed that the stream routing scheme of Rhine
 617 catchment at 0.5° obtained from the forcing data STN-30p (Vörösmarty et al., 2000) differs
 618 significantly from the stream routing scheme extracted based on high resolution (3") DEM (Fig.
 619 S7). Thus, besides the errors in simulated SOC stocks, soil erosion rate, stream discharge rate,
 620 and sediment transport and deposition rate, the inaccurate stream routing scheme used in this
 621 study might also be an important reason for the underestimation of POC concentration in Rhine
 622 river.



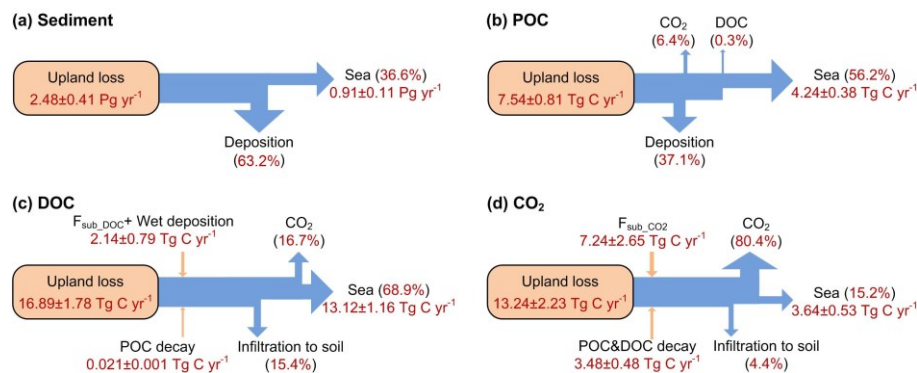
623

624 **Figure 6** Comparison between observed (instantaneous measurements) and simulated (monthly
 625 average values) riverine POC concentrations and POC discharge rates at three gauging sites. The
 626 histograms and error bars denote the means and standard deviations of POC concentrations,
 627 respectively. Long-term average water discharge rates at Bad Honnef, Bimmen and Rheine
 628 during the observation periods are 2023, 2100 and 80 m³ s⁻¹, respectively.

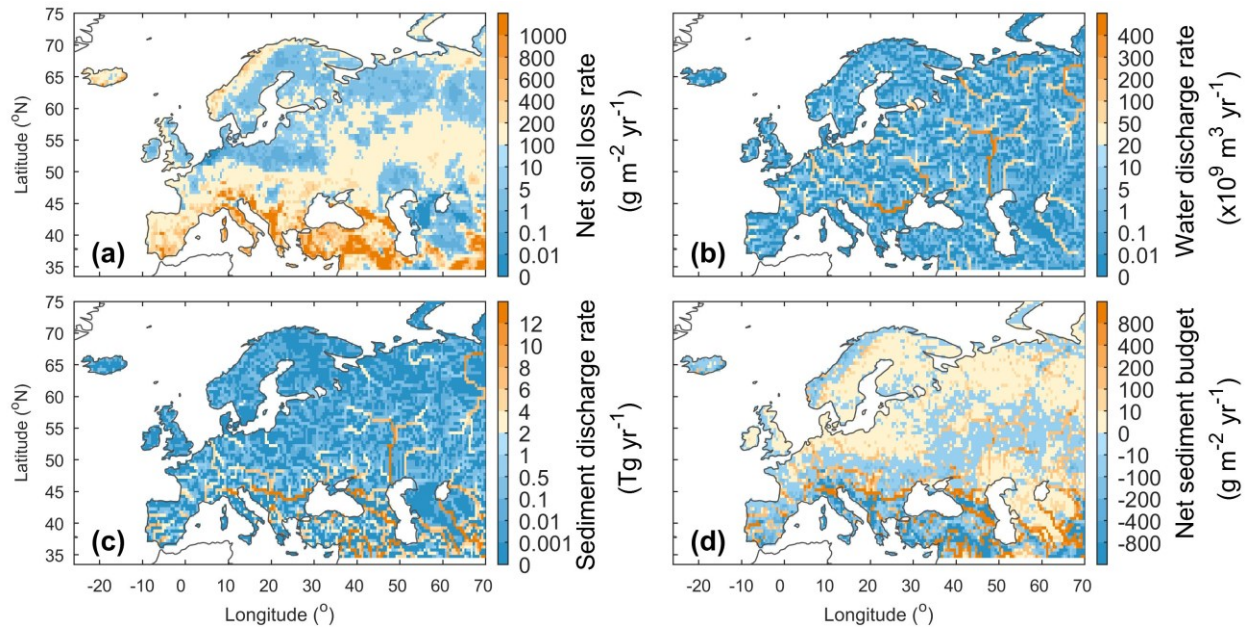
629 3.2 Lateral carbon transfers in Europe

630 Based on our simulation results, the average annual sediment delivery from upland to the river
 631 network caused by water erosion in Europe (-30W– 70E, 34N-75N) during 1901-2014 is 2.8±0.4
 632 Pg yr⁻¹ (Fig. 7a). From Northern to Southern Europe, the sediment delivery rate from upland to
 633 river increase from less than 1.0 g m⁻² yr⁻¹ in the Scandinavia Peninsula, which is covered by
 634 mature boreal forests (Fig. S13a), and in the Northern European Plain to more than 600 g m⁻² yr⁻¹
 635 in the mountainous regions of the Apennine Peninsula, Balkan Peninsula and the Middle East
 636 (Figs. 8a, S14a). The Caucasus is mainly covered by ice and bare rock (Fig. S13), thus the
 637 sediment delivery rate in this region is also very low. In total across Europe, 63.2% (1.8±0.2 Pg
 638 yr⁻¹) of the sediment delivered into river network is deposited in river channels and floodplains,
 639 and the remaining 36.8% (1.0±0.1 Pg yr⁻¹) is exported to the sea (Fig. 7a). Generally, large

640 rivers, like Danube, Volga, and Ob rivers, carry more sediment to the sea than small rivers (Figs.
 641 8b, c). But several relatively small rivers in the Middle East and the Po river in northern Italy
 642 also carry similarly large amount of sediment to the sea, as the upland soil erosion rates are very
 643 high ($> 200 \text{ g m}^{-2} \text{ yr}^{-1}$) in these catchments (Figs. 8a, c). Spatial distribution of the sediment
 644 deposition is controlled by the stream routing scheme and the spatial distribution of floodplains
 645 (Fig. 9b). In Northern and Central Europe, the area-averaged sediment deposition rates (i.e.
 646 amount of annual sediment deposition /area of $0.5^\circ \times 0.5^\circ$ grid cell) in river channels and
 647 floodplains are mostly less than $100.0 \text{ g m}^{-2} \text{ yr}^{-1}$ (Fig. 8d). In the downstream part of the Danube,
 648 Po and several rivers in the Middle East, the sediment deposition rate can exceed $800.0 \text{ g m}^{-2} \text{ yr}^{-1}$
 649 ¹. From 1901 to 1960s, the annual total sediment delivery from uplands to the whole river
 650 network of Europe declined significantly ($p < 0.01$, independent sample t-test) from about 3.0 Pg
 651 yr^{-1} to about 2.3 Pg yr^{-1} (Fig. S15a). From 1960 to 2014, the annual sediment delivery rate did
 652 not show a significant trend, but revealed large interannual variations.



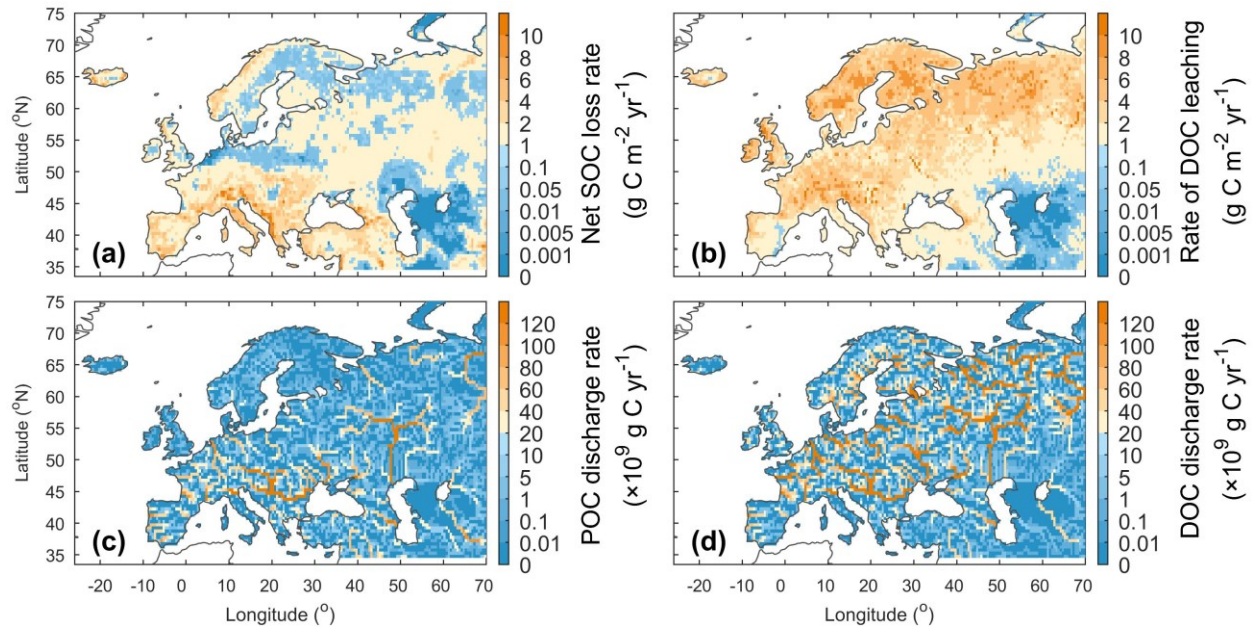
653
 654 **Figure 7** Averaged annual lateral redistribution rate of sediment (a), POC (b), DOC (c) and CO_2
 655 (d) in Europe for the period 1901-2014. $F_{\text{sub_DOC}}$ and $F_{\text{sub_CO}_2}$ are the DOC and CO_2 inputs from
 656 floodplain soil (originated from the decomposition of submerged litter and soil carbon) to the
 657 overlying flooding water, respectively.



658

659 **Figure 8** Averaged annual lateral redistribution rate of water and sediment in Europe during
 660 1901-2014. (a) Annual sediment delivery rate from upland to river network; (b) annual water
 661 discharge rate; (c) annual sediment discharge rate and (d) annual net sediment budget in each
 662 $0.5^{\circ} \times 0.5^{\circ}$ grid cell. In figure d, the positive and negative values denote net gain and net loss of
 663 sediment, respectively.

664 Along with soil erosion and sediment transport, the average annual POC delivery from upland to
 665 river network in the whole Europe during 1901-2014 is $10.1 \pm 1.1 \text{ Tg C yr}^{-1}$ (Fig. 7b). 41.0% of
 666 the POC delivered into the river network is deposited in river channels and floodplains, 2.9% is
 667 decomposed during transport, and the remaining 56.1% is exported to the sea. Spatial patterns of
 668 the area-averaged SOC delivery rate and POC discharge rate basically follow that of sediment
 669 (Fig. 9a, c). Although the sediment discharge rates in some rivers in the Middle East can be as
 670 high as that in the Danube or Volga river (Fig. 8c), the POC delivery rates in these rivers are
 671 much smaller than in the larger ones (Fig. 9c). This is mainly due to the lower SOC stocks in the
 672 Middle East compared to those found in the Danube and Volga catchments (Fig. S8). We also
 673 note that different from the sediment delivery, the annual total POC delivery from upland to river
 674 network in Europe did not show a significant declining trend from 1901 to 1960s (Fig. S15b).
 675 The increase in SOC stock (Fig. S15c) may have partially offset the decline in sediment delivery
 676 rate.



677

678 **Figure 9** Averaged annual lateral redistribution rate of organic carbon in Europe during 1901-
 679 2014. (a) Annual SOC delivery rate from upland to river network; (b) annual DOC leaching rate;
 680 (c) annual POC discharge rate and (d) annual DOC discharge rate.

681 Leaching results in an average annual DOC input of $13.5 \pm 1.5 \text{ Tg C yr}^{-1}$ from soil to the river
 682 network in Europe, and the *in-situ* DOC production caused by wet deposition and the
 683 decomposition of riverine POC and submerged litter and soil organic carbon under flooding
 684 waters amounts to $2.2 \pm 0.7 \text{ Tg C yr}^{-1}$ (Fig. 7c). 28.1% of the total riverine DOC is then infiltrating
 685 into the floodplain soils, 12.9% is decomposed during riverine transport, and the remaining
 686 59.0% is exported to the sea. The spatial distribution of the DOC leaching rate is very different
 687 from that of POC (Fig. 9b). From North-western Europe to Southeast Europe and the Middle
 688 East, the DOC leaching rates decrease from over $6 \text{ g C m}^{-2} \text{ yr}^{-1}$ to less than $1.0 \text{ g C m}^{-2} \text{ yr}^{-1}$. DOC
 689 discharge rates in major European rivers, such as Rhine, Danube, Volga, Elbe and Ob, are mostly
 690 higher than 100 Tg C yr^{-1} (Fig. 9d). Comparatively, the DOC discharge rates in Southern Europe
 691 and the Middle East are significantly lower ($< 60 \text{ Tg C yr}^{-1}$).

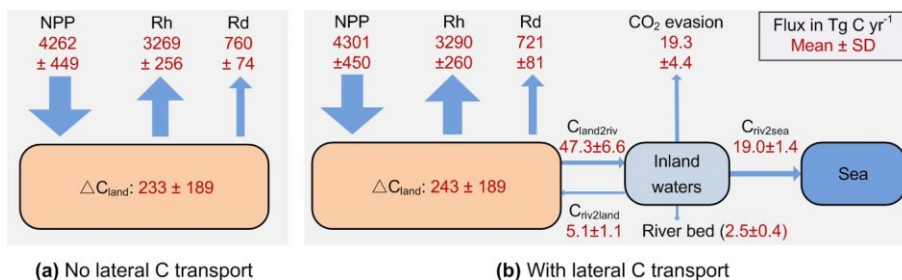
692 The average annual leaching rate of CO_2 sourced from the decomposition of upland litter and
 693 soil organic carbon (incl. DOC) in the whole Europe is $14.3 \pm 2.2 \text{ Tg C yr}^{-1}$ (Fig. 7a).

694 Decomposition of the submerged litter and organic carbon in floodplains and the decomposition
 695 of riverine POC and DOC add an *in-situ* CO_2 production amounting to $7.5 \pm 2.7 \text{ Tg C yr}^{-1}$ and

696 4.1±0.5 Tg C yr⁻¹, respectively. Most of this CO₂ (80.2%) feeding stream waters is then released
 697 back to the atmosphere quickly, in such a way that only 15.8% of the CO₂ is exported to the sea,
 698 and 4.0% is infiltrated into the floodplain soils.

699 3.3 Implications for the terrestrial C budget of Europe

700 Representing the lateral carbon transport in LSM is helpful to estimate the terrestrial carbon
 701 cycle more accurately. From the year 1901 to 2014, soil erosion and leaching combined resulted
 702 in a 5.4 Pg loss of terrestrial carbon to the European river network, this amount corresponding to
 703 about 5% of the total SOC stock (106 Pg C, Fig. S8a) in the 0-30 cm soil layer. The average
 704 annual total delivery of organic carbon (POC+DOC) during the same period is 47.3±6.6 Tg C yr⁻¹
 705 (Fig. 7), which is about 4.7% of the net ecosystem production (NEP (993±255 Tg C yr⁻¹),
 706 defined as the difference between the vegetation primary production (NPP) and the soil
 707 heterotrophic respiration (Rh) due to the decomposition of litter and soil organic matter, i.e.
 708 NEP=NPP–Rh), and 19.2% of the net biome production (NBP (243±189 Tg C yr⁻¹), defined as
 709 the difference between NEP and the land carbon loss (Rd) due to the additional disturbances (e.g.
 710 harvest, land cover change, and soil erosion and leaching, i.e. NBP=NEP–Rd–DOC and POC to
 711 river) (Fig. 10b). The annual total export of carbon to the sea surrounding Europe is 19.0±1.4 Tg
 712 C yr⁻¹, which amounts to 1.9% and 8.7% of the NEE and NBP, respectively.



713
 714 **Figure 10** The simulated average annual carbon budget of the terrestrial ecosystem in Europe
 715 during the 1901-2014 when the lateral carbon transport is ignored (a) and considered (b). All
 716 fluxes are presented as mean ± standard deviation. NPP is the net primary production. Rh and Rd
 717 are the heterotrophic respiration and the respiration due to disturbances like harvest and land
 718 cover change, respectively. ΔC_{land} is the average annual changes of the total land carbon stock.
 719 Percentage following each of these changes in blue is the average annual relative changes of the
 720 corresponding carbon pool. C_{land2riv}, C_{riv2land} and C_{riv2sea} are the average annual carbon fluxes

721 from land to inland waters, from inland waters to floodplains and from inland waters to the sea,
722 respectively. SD is the standard deviation.

723 Besides direct transfers of organic carbon from soil to aquatic systems, the lateral transport of
724 water, sediment and carbon can also affect the land carbon budget through several indirect ways.
725 First, the lateral redistribution of surface runoff can affect the land carbon budget by altering soil
726 wetness. Our simulation results reveal that the lateral redistribution of runoff can significantly
727 change local soil wetness, especially in floodplains (Fig. S14b), where the increase in soil
728 wetness can be larger than 10% (Fig. S17b). Soil wetness is a key controlling factor of plant
729 photosynthesis (Knapp et al., 2001; Stocker et al., 2019; Xu et al., 2013). Benefiting from the
730 increase in soil wetness, the NPP in many grid cells with a large area of floodplain has increased
731 by more than 5% (Fig. 10b), although the NPP over the whole Europe only increased by 1%
732 (Fig. 10). Changes in soil wetness can further alter soil temperature (Fig. S17a). As soil wetness
733 and temperature are the two most important controlling factors of organic matter decomposition,
734 the lateral redistribution of runoff can affect local land carbon budget by changing the Rh.
735 Moreover, in ORCHIDEE-C_{lateral}, the turnover times of litter and SOC under flooding waters
736 (assumed to experience anaerobic condition) are set to be one third of the litter and SOC turnover
737 times in upland soil (Reddy & Patrick Jr, 1975; Neckles & Neill, 1994; Lauerwald et al., 2017).
738 Accounting for flooding thus decreases the decomposition rate of litter and SOC stored in
739 floodplain soils.

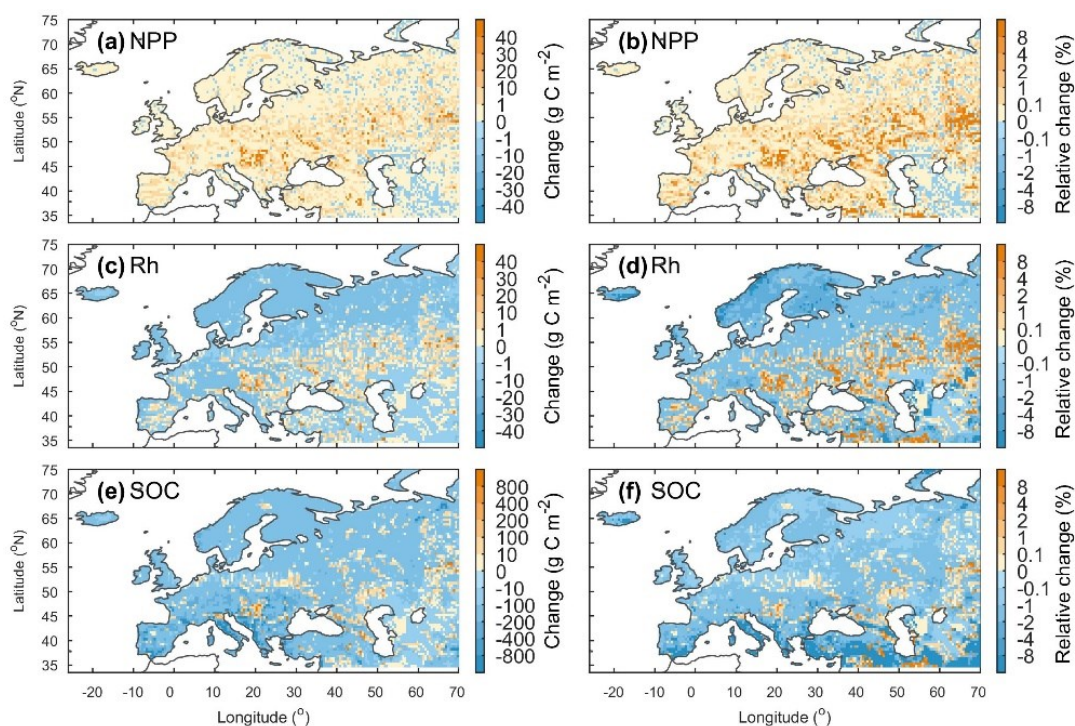
740 Second, soil erosion and sediment deposition can affect land carbon budget by altering the
741 vertical distribution of litter and soil organic carbon. At the net erosion sites of the uplands, the
742 loss of surface soil results in a part of the belowground litter and SOC that were originally stored
743 in deeper soil layers emerging to the surface soil layers, and also results in a fraction of the
744 belowground litter becoming the aboveground litter. In the floodplains, the newly deposited
745 sediment becomes part of the surface soil layer, and the belowground litter and SOC in the
746 original surface soil layer is transferred down to the deeper soil layers. As the temperatures and
747 fresh organic matter inputs (sourced from the aboveground litterfall and dead roots), which can
748 impact SOC decomposition rates through the priming effect (Guenet et al., 2016; Guenet et al.,
749 2010), in different soil layers are different, changes in the vertical distribution of belowground

750 litter and SOC can therefore lead to changes in the overall decomposition rate of the organic
751 matter in the whole soil column.

752 Third, soil aggregates mostly break down during soil erosion and sediment transport, the riverine
753 POC thus loses part of its physical protection from decomposition (Hu and Kuhn, 2016; Lal,
754 2003). Some modelling studies have assumed that at least 20% of the eroded SOC would be
755 decomposed during the soil erosion and transport processes (Lal, 2003, 2004; Zhang et al.,
756 2014). However, the estimation by Smith et al. (2001) using a conceptual mass balance model
757 suggest that only a tiny fraction of the eroded POC is decomposed and released as CO₂ to the
758 atmosphere. Using laboratory rainfall-simulation experiments, van Hemelryck et al. (2010)
759 estimated a 2%-12% mineralization of the eroded SOC from a loess soil, and Wang et al. (2014)
760 estimated a mineralization of only 1.5%. In ORCHIDEE-C_{lateral}, the passive SOC pool is
761 regarded as the SOC associated to soil minerals and protected by soil aggregates. The turnover
762 time of the passive POC in river stream and flooding waters is assumed to be same to that of the
763 active POC (0.3 year). Our simulation results suggest that the fraction of total riverine POC that
764 is decomposed during the lateral transport from uplands to the sea is 2.9% in Europe (Fig. 7b),
765 which is larger than the POC decomposition fraction (0.9%) when the turnover time of the
766 passive POC in rivers is assumed to be same to that of the passive POC (i.e. no soil aggregates
767 break down). The acceleration of POC decomposition rate due to the breakdown of soil
768 aggregates can thus slightly affect the estimate of the regional land-atmosphere carbon flux.
769 Moreover, the riverine POC and DOC can be transported over a long distance and finally settle
770 or infiltrate in floodplains or river channels (especially the Estuarine deltas) where the local
771 environmental conditions might be quite different from those encountered in the uplands from
772 where these C pools originate. These changes in environmental conditions can affect the
773 decomposition rate of the laterally redistributed organic carbon (Abril et al., 2002).

774 Comparison between the simulation results from ORCHIDEE-C_{lateral} with activated and
775 deactivated erosion and river routing modules indicate that ignoring lateral carbon transport
776 processes in LSM may lead to significant biases in the simulated land carbon budget (Figs. 10
777 and S15). Although the omission of lateral carbon transport in ORCHIDEE-C_{lateral} only resulted
778 in a 1% decrease in simulated average annual total NPP in Europe during 1901-2014 and a 1%
779 increase of annual total Rh, the annual total NBP (=NEP-Rd-DOC and POC to river) is

780 overestimated by 4.5%. Over the same period, the lateral carbon transport only induced a 0.09%
 781 decrease in the total SOC and DOC stock in Europe (Fig. S16c), but their spatial distribution was
 782 significantly altered (Figs. 11e,f). For instance, in some mountainous regions, the soil erosion
 783 induced a reduction of the SOC stock by more than 8%. On the contrary, the sediment and POC
 784 deposition in some floodplains led to an increase in SOC stock by more than 8% (Fig. 11f).



785

786 **Figure 11** Changes (first column) and relative changes (second column) of the net primary
 787 production (NPP), heterotrophic respiration (Rh) and total soil organic carbon (SOC, 0-2 m) in
 788 Europe due to the lateral carbon transport during 1901-2014. For each variable, the change is
 789 calculated as $C_{lat} - C_{nolat}$, where C_{lat} and C_{nolat} are the carbon fluxes or stocks when lateral carbon
 790 transport is considered and ignored, respectively. The relative changes is calculated as $(C_{lat} -$
 791 $C_{nolat}) / C_{nolat} \times 100\%$.

792 Consistent with previous studies (Stallard, 1998; Smith et al., 2001; Hoffmann et al., 2013), our
 793 simulation results reveal the importance of sediment deposition in floodplains for the overall
 794 SOC budget. From 1901 to 2014, erosion and leaching over Europe totally induced a loss of 3.03
 795 Pg organic carbon (POC+DOC) from uplands to the river network, and only 0.65 Pg of this
 796 carbon was redeposited onto the floodplains. The total stock of soil organic carbon in Europe
 797 thus should have decreased by 2.38 Pg C. However, due to the decrease in decomposition rate of

798 the buried organic carbon (including in-situ and ex-situ carbon) in floodplain soils, the total stock
799 of soil organic carbon in Europe only decreased by 0.91 Pg C. Floodplains in Europe have totally
800 protected 2.12 (= 3.03 - 0.91) Pg soil organic carbon from been transported to the sea or be
801 released to the atmosphere in forms of CO₂. Although the sequestration of organic carbon in
802 floodplains cannot make up all of the soil organic carbon (POC+DOC) loss, the increased
803 organic carbon stock in floodplains (2.12 Pg C) is much higher than the soil POC loss (0.86 Pg
804 C) induced by soil erosion.

805 **3.4 Uncertainties and future work**

806 In the present version of ORCHIDEE-C_{lateral}, the lateral transfers of sediment and carbon is
807 simulated using a simplified scheme, due to the fragmented nature of large-scale forcing (e.g.
808 geomorphic properties of the river channel) and validation data (e.g. continuous sediment and
809 carbon concentration data in river streams and deposition/erosion rates in river channels). We
810 recognize that this simplification induces significant uncertainties in model outputs, especially
811 regarding changes in lateral sediment and particulate carbon transfers under climate change and
812 direct human perturbations. Several physics-based algorithms have been proposed to accurately
813 calculate the *TC* of stream flows (Arnold et al., 1995; Molinas and Wu, 2001; Nearing et al.,
814 1989). These algorithms mostly require detailed information about the stream power (e.g. flow
815 speed and depth), geomorphic properties of the river channel (e.g. slope and hydraulic radius)
816 and the physical properties of the sediment particles (e.g. median grain size) (Neitsch et al.,
817 2011). They are good predictors to estimate *TC* in rivers with detailed observation data on local
818 stream, soil, geomorphic properties. Unfortunately, it is not practical to implement those
819 algorithms in ORCHIDEE-C_{lateral} due to the lack of appropriate forcing data at large scale as well
820 as the relatively rough representation of stream flow dynamics compared to hydrological models
821 for small basins. For example, runoff and sediment from all headwater basins in one 0.5° grid
822 cell of ORCHIDEE-C_{lateral} are assumed to flow into one single virtual river channel. Although
823 the total river surface area in each grid cell is represented (obtained from forcing file (Table 1),
824 Lauerwald et al., 2015), the length, width and depth of the river channel are unknown.
825 Furthermore, in reality, there can be multiple river channels in the area represented by each grid
826 cell, and these channels might flow to different directions.

827 We also noticed that previous studies have derived empirical functions of upstream drainage area
828 (e.g. Luo et al., 2017) or upstream runoff (e.g. Yamazaki et al., 2011) to calculate the river width
829 and depth, allowing to simulate the water flow in the river channel using physically-based
830 algorithms. Unfortunately, to obtain a good fit of the simulated river discharges against
831 observations, the parameters in the empirical functions for calculating river width and depth
832 generally need to be calibrated separately for each catchment (Luo et al., 2017), an approach that
833 is incompatible with large-scale simulations like those performed here. Without such calibration,
834 the simulated geometrical properties of the river channel and runoff are prone to large
835 uncertainties, thus rendering the simulation of sediment transport at continental or global scale
836 using physically-based algorithms a more challenging task. Given the difficulty to simulate the
837 detailed hydraulic dynamics of the stream flow at large spatial scale, we thus apply a simple
838 approach described below to calculate the sediment transport capacity. Overall, we encourage
839 future studies to produce large-scale databases on the geomorphic properties of global river
840 channels (e.g. river depth and width) and to develop large-scale sediment transport models which
841 can give a capable of producing more realistic and accurate simulations of sediment deposition,
842 re-detachment and transport processes, as well as including the exchanges of water, sediment and
843 carbon between river stream and floodplains.

844 The simulation of the soil DOC dynamics and leaching in our model need to be further improved
845 to better simulate the seasonal variation of riverine DOC and TOC concentrations. The
846 concentration of soil DOC and the DOC decomposition rate during the lateral transport process
847 in the river network are the two key factors controlling DOC concentration in river flow. As
848 only a small fraction ($< 20\%$) of the riverine DOC is decomposed during lateral transport (Fig.
849 7), the overestimated (Fig. 5) seasonal amplitude in riverine DOC (and TOC) concentrations is
850 likely caused by the uncertainties in the simulated seasonal dynamics of the leached soil DOC.
851 The current scheme used in our model for simulating soil DOC dynamics has been calibrated
852 against observed DOC concentrations at several sites in Europe (Camino-Serrano et al., 2018).
853 Although the calibrated model can overall capture the average concentrations of soil DOC, it is
854 not able to fully capture the temporal dynamics of DOC concentrations (Camino-Serrano et al.,
855 2018). Given this, it is necessary to collect additional observation data on the seasonal dynamics
856 of soil DOC concentration to further calibrate the soil DOC model. In addition, averaged over
857 the various DOC and SOC pools we distinguish in the soils, DOC represents a much more

858 reactive fraction of soil carbon (with a turnover time of several days to a few months) than SOC
859 (with a turnover time of decades to thousands of years). Therefore, soil DOC concentrations
860 experience large seasonal variations, while SOC concentrations generally are much more stable
861 and show very limited seasonal dynamics. Overall, seasonal variations in riverine POC
862 concentrations are mainly controlled by the seasonal dynamics of soil erosion rates, rather than
863 by the seasonal SOC dynamics, which explains a partial decoupling in the behavior of POC
864 compared to that of DOC.

865 Although most processes related to lateral carbon transport have been represented in
866 ORCHIDEE-C_{lateral}, there are still omitted processes and large uncertainties in our model. For
867 example, many studies suggest that a substantial portion of the eroded sediment and carbon is
868 deposited downhill at adjacent lowlands as colluviums, rather than exported to the river (Berhe et
869 al., 2007; Smith et al., 2001; Hoffmann et al., 2013; Wang et al., 2010). As the deposition of
870 sediment and carbon within headwater basins can also significantly alter the vertical SOC profile
871 and soil micro-environments (e.g. soil moisture, aeration and density) (Doetterl et al., 2016;
872 Gregorich et al., 1998; Wang et al., 2015; Zhang et al., 2016), omission of this process may
873 result in uncertainties in the simulated vegetation production and SOC decomposition. In
874 addition, the impact of artificial dams and reservoirs on riverine sediment and carbon fluxes is
875 also not represented in our model. Construction of dams generally leads to increased water
876 residence time, nutrient retention, and sediment and carbon trapping in the impounded reservoir
877 (Maavara et al., 2017), and can also affect the downstream flooding regime and frequency (Mei
878 et al., 2016; Timpe and Kaplan, 2017). Estimation by Maavara et al. (2017) suggests that the
879 organic carbon trapped or mineralized in global artificial reservoirs is about 13% of the total
880 organic carbon carried by global rivers to the oceans. To more accurately simulate the lateral
881 carbon transport, we plan to include the soil and carbon redistribution within headwater basins
882 and the effects of dams and reservoirs on riverine sediment and carbon fluxes into our model in
883 the near future.

884 The effects of lateral redistribution of water and sediment on vegetation productivity has not
885 been fully represented in our model. As shown above, our model is able to represent the impacts
886 of lateral water redistribution on vegetation productivity though modifying local soil wetness
887 (Figs. 11 and S17). However, in addition to modifying soil wetness, many studies have indicated

888 that the soil erosion and sediment deposition can affect vegetation productivity by modifying soil
889 nutrient (e.g. nitrogen (N) and phosphorus (P)) availability (Bakker et al., 2004; Borrelli et al.,
890 2018; Quine, 2002; Quinton et al., 2010). Recently, terrestrial N and P cycles have already been
891 incorporated into another branch of ORCHIDEE (i.e. the ORCHIDEE-CNP developed by Goll et
892 al., 2017). By coupling our new branch and ORCHIDEE-CNP, it will be possible to develop a
893 more comprehensive LSM that can also simulate the effects of lateral N and P redistribution on
894 vegetation productivity.

895 Although soils are the major source of riverine organic carbon, domestic, agricultural and
896 industrial wastes, as well as river-borne phytoplankton can also make significant contributions
897 (Abril et al., 2002; Meybeck, 1993; Hoffmann et al., 2020). Moreover, previous studies have
898 shown that sewage generally contains highly labile POC while most of the aquatic production is
899 generally mineralized within a short time (Abril et al., 2002; Caffrey et al., 1998). Omission of
900 organic carbon inputs from manure and sewage could potentially lead to an underestimation of
901 CO₂ evasion from the European river network. Inclusion of these additional carbon sources
902 should thus help improve simulation of aquatic CO₂ evasion.

903 Uncertainties in our simulation results also stem from the forcing data (Table 1) applied in our
904 model. The routing scheme of water, sediment and carbon is driven by a map of stream flow
905 direction at 0.5° spatial resolution (Guimberteau et al., 2012). Comparison between this flow
906 direction map and the flow direction map derived based on high resolution (3") DEM show
907 discrepancies between the two river flow networks (Fig. S7). As the flow direction directly
908 determines the area of each catchment and the route of river flows, errors in forcing data of flow
909 direction may thus induce uncertainties in the simulated riverine water, sediment and carbon
910 discharges. Land-cover maps are another source of uncertainty. For instance, croplands generally
911 experience significantly larger soil erosion rates than grasslands and forests (Borrelli et al., 2017;
912 Nunes et al., 2011; Zhang et al., 2020). However, croplands in ORCHIDEE are only represented
913 in a simplified way by segmenting them into C3 and C4 crops based on their photosynthesis
914 characteristics. Therefore, our simulations based on land cover data with only two broad groups
915 of crop might not be able to fully capture the seasonal dynamics of planting, canopy growth rate
916 and harvesting for all crop types. Furthermore, the effects of soil conservation practices, which
917 would decrease erosion rates, are ignored in our model. Panagos et al. (2015) have shown that

918 contour farming, stone wall and grass margin techniques have been applied in Europe reduce the
919 risk of soil erosion. However, these soil conservation practices only reduce the average erosion
920 rate in European Union by 3%. Excluding soil conservation practices thus should have limited
921 impact in our simulation results.

922 Further model calibration, evaluation and development is necessary for improving our model.
923 Due to the limitation of observation data, we calibrated the parameters controlling sediment
924 transport, deposition and re-detachment (i.e. ω , C_{rivdep} , C_{flddep} , C_{ebed} and C_{ebank} in Table S1) in
925 stream and flooding reservoirs only against the observed sediment yield. Even though our model
926 can overall capture the lateral transfers of sediment and carbon in many rivers in central and
927 northern Europe, more observation data are crucially needed to further evaluate the performance
928 of our model, in particular in southern Europe. In addition, it is still unknown whether our model
929 can satisfactorily simulate intermediate processes such as sediment deposition in river channels
930 and floodplains, as well as the rate of river channel erosion. It is also unknown whether our
931 model would perform satisfactorily in regions with very different climates than Europe such as
932 the tropical region. Thus, in the future, an important aim will be to further calibrate our model
933 against more detailed observation data (e.g. sediment deposition rate in river channels and
934 floodplains) and extend the model application to regions of contrasting climate, vegetation and
935 topography. Moreover, the GLORICH database (Hartmann et al., 2019) only provides
936 instantaneous observations of riverine organic carbon concentrations and it is therefore difficult
937 to evaluate the model's ability to reproduce temporal trends. Therefore, future modelling efforts
938 should be combined with data mining efforts targeting the collection of continuous (e.g. daily)
939 and long-term observational data of organic carbon content and fluxes in streams and rivers.

940

941 **Conclusions**

942 By merging ORCHILEAK (Lauerwald et al., 2017) and an upgraded version of ORCHIDEE-
943 MUSLE (Zhang et al., 2020) for the simulation of DOC and POC from land to sea, respectively,
944 we developed ORCHIDEE-C_{lateral}, a new branch of the ORCHIDEE LSM. ORCHIDEE-C_{lateral}
945 simulates the large-scale lateral transport of water, sediment, POC, DOC and CO₂ from uplands
946 to the sea through river networks, the deposition of sediment and POC in river channels and
947 floodplains, the decomposition POC and DOC during fluvial transport and the CO₂ evasion to

948 the atmosphere, as well as the changes in soil wetness and vertical SOC profiles due to the lateral
949 redistribution of water, sediment and carbon.

950 Evaluation using observation data from European rivers indicate that ORCHIDEE-C_{lateral} can
951 satisfactorily reproduce the observed riverine discharges of water and sediment, bankfull flows
952 and organic carbon concentrations in river flows. Application of ORCHIDEE-C_{lateral} to the entire
953 European river network from 1901 to 2014 reveals that the average annual total carbon delivery
954 to streams and rivers amounts to $47.3 \pm 6.6 \text{ Tg C yr}^{-1}$, which corresponds to about 4.7% of total
955 NEP and 19.2% of the total NBP of terrestrial ecosystems in Europe. The lateral transfer of
956 water, sediment and carbon can affect the land carbon dynamics through several different
957 mechanisms. Besides directly inducing a spatial redistribution of organic carbon, it can also
958 affect the regional land carbon budget by altering vertical SOC profiles, as well as the soil
959 wetness and soil temperature, which in turn impact vegetation production and the decomposition
960 of soil organic carbon. Overall, omission of lateral carbon transport in ORCHIDEE potentially
961 results in an underestimation of the annual mean NBP in Europe of 4.5%. In regions
962 experiencing high soil erosion or high sediment deposition rate, the lateral carbon transport also
963 changes total SOC stock significantly, by more than 8%.

964 We recognize that ORCHIDEE-C_{lateral} is still entailed with several limitations and significant
965 uncertainties. To address those, we plan to enhance our model with additional processes, such as
966 sediment deposition at downhills or the regulation of lateral transport by dams and reservoirs.
967 We also plan to calibrate and evaluate further our model by extending the observational dataset
968 to regions outside Europe.

969

970 **Code and data availability**

971 The source code of ORCHIDEE-Clateral model developed in this study is available online
972 (<https://doi.org/10.14768/f2f5df9f-26da-4618-b69c-911f17d7e2ed>) from 22 July, 2019. All
973 forcing and validation data used in this study are publicly available online. The specific sources
974 for these data can be found in section Table 1.

975

976 **Author contributions**

977 HZ, RL and PR designed the study. HZ and RL conducted the model development and
978 simulation experiments. PR, KV, PC, VN, BG and WY provided critical contribution to the
979 model development and the design of simulation experiments. HZ conducted the model
980 calibration, validation and the data analysis. RL, PR, PC, KV and BG provided support on
981 collecting forcing and validation data. HZ, RL and PR wrote the manuscript. All authors
982 contributed to interpretation and discussion of results and improved the manuscript.

983

984 **Competing interests**

985 The contact author has declared that neither they nor their co-authors have any competing
986 interests.

987

988 **Acknowledgements**

989 HZ and PR acknowledges the ‘Lateral-CNP’ project (No. 34823748) supported by the Fonds de
990 la Recherche Scientifique –FNRS and the VERIFY project that received funding from the
991 European Union’s Horizon 2020 research and innovation program under grant agreement No.
992 776810. RL and PC acknowledge funding by the French state aid managed by the ANR under
993 the "Investissements d'avenir" programme [ANR-16-CONV-0003_Cland]. P.R. received funding
994 from the European Union’s Horizon 2020 research and innovation programme under Grant
995 Agreement no. 101003536 (ESM2025 – Earth System Models for the Future).

996

998 **References:**

- 999 Abotalib, A. Z., and Mohamed, R. S. A.: Surface evidences supporting a probable new concept for the river systems
1000 evolution in Egypt: a remote sensing overview. *Environ. Earth Sci.*, 69, 1621-1635, 2012.
- 1001 Abrams, M., Crippen, R., and Fujisada, H.: ASTER Global Digital Elevation Model (GDEM) and ASTER Global
1002 Water Body Dataset (ASTWBD). *Remote Sens.*, 12, 2020.
- 1003 Abril, G., Nogueira, M., Etcheber, H., Cabecadas, G., Lemaire, E., and Brogueira, M. J.: Behaviour of organic
1004 carbon in nine contrasting European estuaries. *Estuar., Coast. Shelf Sci.*, 54, 241-262, 2002.
- 1005 Arnold, J. G., Williams, J. R., and Maidment, D. R.: Continuous-time water and sediment-routing model for large
1006 basins. *J. Hydraul. Eng.*, 121, 171-179, 1995.
- 1007 Bakker, M. M., Govers, G., and Rounsevell, M. D. A.: The crop productivity–erosion relationship: an analysis based
1008 on experimental work. *Catena*, 57, 55-76, 2004.
- 1009 Battin, T. J., Luysaert, S., Kaplan, L. A., Aufdenkampe, A. K., Richter, A., and Tranvik, L. J.: The boundless
1010 carbon cycle. *Nat. Geosci.e*, 2, 598-600, 2009.
- 1011 Berhe, A. A., Harte, J., Harden, J. W., and Torn, M. S.: The Significance of the Erosion-induced Terrestrial Carbon
1012 Sink. *BioScience*, 57, 337-346, 2007.
- 1013 Beusen, A. H. W., Dekkers, A. L. M., Bouwman, A. F., Ludwig, W., and Harrison, J.: Estimation of global river
1014 transport of sediments and associated particulate C, N, and P. *Global Biogeochem. Cycles*, 19,
1015 <https://doi.org/10.1029/2005GB002453>, 2005.
- 1016 Borrelli, P., Robinson, D. A., Fleischer, L. R., Lugato, E., Ballabio, C., Alewell, C., Meusburger, K., Modugno, S.,
1017 Schütt, B., Ferro, V., Bagarello, V., Oost, K. V., Montanarella, L., and Panagos, P.: An assessment of the
1018 global impact of 21st century land use change on soil erosion. *Nat. Commun.*, 8, 2017.
- 1019 Borrelli, P., Van Oost, K., Meusburger, K., Alewell, C., Lugato, E., and Panagos, P.: A step towards a holistic
1020 assessment of soil degradation in Europe: Coupling on-site erosion with sediment transfer and carbon fluxes.
1021 *Environ. Res.*, 161, 291-298, 2018.
- 1022 Caffrey, J. M., Coloern, J. E., and Grenz, C.: Changes in production and respiration during a spring phytoplankton
1023 bloom in San Francisco Bay, California, USA: implications for net ecosystem metabolism. *Mar. Ecol. Prog.*
1024 *Ser.*, 172, 1-12, 1998.
- 1025 Camino-Serrano, M., Guenet, B., Luysaert, S., Ciais, P., Bastrikov, V., De Vos, B., Gielen, B., Gleixner, G., Jorret-
1026 Puig, A., Kaiser, K., Kothawala, D., Lauerwald, R., Peñuelas, J., Schrumppf, M., Vicca, S., Vuichard, N.,
1027 Walmsley, D., and Janssens, I. A.: ORCHIDEE-SOM: modeling soil organic carbon (SOC) and dissolved
1028 organic carbon (DOC) dynamics along vertical soil profiles in Europe. *Geosci. Model Dev.*, 11, 937-957, 2018.
- 1029 Campoy, A., Ducharne, A., Cheruy, F., Hourdin, F., Polcher, J., and Dupont, J. C.: Response of land surface fluxes
1030 and precipitation to different soil bottom hydrological conditions in a general circulation model. *J. Geophys.*
1031 *Res.: Atmos.*, 118, 10,725-710,739, 2013.
- 1032 Castro, J. M., and Thorne, C. R.: The stream evolution triangle: Integrating geology, hydrology, and biology. *River*
1033 *Res. Appl.*, 35, 315-326, 2019.
- 1034 Chaplot, V. A. M., Rumpel, C., and Valentin, C.: Water erosion impact on soil and carbon redistributions within

1035 uplands of Mekong River. *Global Biogeochem. Cycles*, 19, GB4004, 2005.

1036 Chappell, A., Baldock, J., and Sanderman, J.: The global significance of omitting soil erosion from soil organic
1037 carbon cycling schemes. *Nat. Clim. Chang.*, 6, 187-191, 2016.

1038 Chini, L. P., Hurtt, G. C., and Frohling, S.: Harmonized Global Land Use for Years 1500 – 2100, V1. Data set.
1039 Available on-line [<http://daac.ornl.gov>] from Oak Ridge National Laboratory Distributed Active Archive
1040 Center, Oak Ridge, Tennessee, USA, <http://dx.doi.org/10.3334/ORNLDAAC/1248>, 2014.

1041 Ciais, P., Sabine, C., Bala, G., Bopp, L., Brovkin, V., Canadell, J., Chhabra, A., DeFries, R., Galloway, J., Heimann,
1042 M., Jones, C., Le Quéré, C., Myneni, R. B., Piao, S. L., and Thornton, P.: Carbon and Other Biogeochemical
1043 Cycles, in: Stocker, T. F., Qin, D., Plattner, G.-K., Tignor, M., Allen, S. K., Boschung, J., Nauels, A., Xia, Y.,
1044 Bex, V., and Midgley, P. M. (Eds.), *Climate Change 2013: The Physical Science Basis. Contribution of*
1045 *Working Group I to the Fifth Assessment Report of the Intergovernmental Panel on Climate Change*
1046 Cambridge University Press, Cambridge, United Kingdom and New York, NY, USA, 2013.

1047 Ciais, P., Yao, Y., Gasser, T., Baccini, A., Wang, Y., Lauerwald, R., Peng, S., Bastos, A., Li, W., Raymond, P. A.,
1048 Canadell, J. G., Peters, G. P., Andres, R. J., Chang, J., Yue, C., Dolman, A. J., Haverd, V., Hartmann, J.,
1049 Laruelle, G., Konings, A. G., King, A. W., Liu, Y., Luysaert, S., Maignan, F., Patra, P. K., Pregon, A.,
1050 Regnier, P., Pongratz, J., Poulter, B., Shvidenko, A., Valentini, R., Wang, R., Broquet, G., Yin, Y.,
1051 Zscheischler, J., Guenet, B., Goll, D. S., Ballantyne, A. P., Yang, H., Qiu, C., and Zhu, D.: Empirical estimates
1052 of regional carbon budgets imply reduced global soil heterotrophic respiration. *Natl. Sci. Rev.*, 8,
1053 <https://doi.org/10.1093/nsr/nwaa145>, 2021.

1054 Cohen, S., Kettner, A. J., and Syvitski, J. P. M.: Global suspended sediment and water discharge dynamics between
1055 1960 and 2010: Continental trends and intra-basin sensitivity. *Glob. Planet. Change*, 115, 44-58, 2014.

1056 Cole, J. J., Prairie, Y. T., Caraco, N. F., McDowell, W. H., Tranvik, L. J., Striegl, R. G., Duarte, C. M., Kortelainen,
1057 P., Downing, J. A., Middelburg, J. J., and Melack, J.: Plumbing the Global Carbon Cycle: Integrating Inland
1058 Waters into the Terrestrial Carbon Budget. *Ecosystems*, 10, 172-185, 2007.

1059 Coulthard, T. J., and Van de Wiel, M. J.: Modelling river history and evolution. *Philosophical Transactions A*
1060 *Mathematical, Phys. Eng. Sci.*, 370, 2123-2142, 2012.

1061 d’Orgeval, T., Polcher, J., and de Rosnay, P.: Sensitivity of the West African hydrological cycle in ORCHIDEE to
1062 infiltration processes, *Hydrol. Earth Syst. Sci.*, 12, 1387–1401, <https://doi.org/10.5194/hess-12-1387-2008>,
1063 2008.

1064 Dirmeyer, P. A., Gao, X., Zhao, M., Guo, Z., Oki, T., and Hanasaki, N.: GSWP-2: Multimodel Analysis and
1065 Implications for Our Perception of the Land Surface. *Bull. Amer. Meteorol. Soc.*, 87, 1381-1398, 2006.

1066 Doetterl, S., Berhe, A. A., Nadeu, E., Wang, Z., Sommer, M., and Fiener, P.: Erosion, deposition and soil carbon: A
1067 review of process-level controls, experimental tools and models to address C cycling in dynamic landscapes.
1068 *Earth Sci. Rev.*, 154, 102-122, 2016.

1069 Drake, T. W., Raymond, P. A., and Spencer, R. G. M.: Terrestrial carbon inputs to inland waters: A current
1070 synthesis of estimates and uncertainty. *Limn.Oceanogr. Lett.*, 3, 132-142, 2018.

1071 FAO/IASA/ISRIC/ISSCAS/JRC: Harmonized World Soil Database (version 1.2), FAO, Rome, Italy and IASA,

1072 Laxenburg, Austria, 2012.

1073 Galy, V., France-Lanord, C., and Lartiges, B.: Loading and fate of particulate organic carbon from the Himalaya to
1074 the Ganga–Brahmaputra delta. *Geochim. Cosmochim. Acta*, 72, 1767-1787, 2008.

1075 Gassman, P. W., Sadeghi, A. M., and Srinivasan, R.: Applications of the SWAT Model Special Section: Overview
1076 and Insights. *J. Environ. Qual.*, 43, 1-8, 2014.

1077 Gregorich, E. G., Greer, K. J., Anderson, D. W., and Liang, B. C.: Carbon distribution and losses: erosion and
1078 deposition effects. *Soil Tillage Res.*, 47, 291-302, 1998.

1079 Guenet, B., Camino-Serrano, M., Ciais, P., Tifafi, M., Maignan, F., Soong, J. L., and Janssens, I. A.: Impact of
1080 priming on global soil carbon stocks. *Glob. Change Biol.*, 24, 1873-1883, 2018.

1081 Guenet, B., Moyano, F. E., Peylin, P., Ciais, P., and Janssens, I. A.: (2016) Towards a representation of priming on
1082 soil carbon decomposition in the global land biosphere model ORCHIDEE (version 1.9.5.2). *Geosci. Model
1083 Dev.*, 9, 841-855, 2016.

1084 Guenet, B., Neill, C., Bardoux, G., and Abbadie, L.: Is there a linear relationship between priming effect intensity
1085 and the amount of organic matter input? *Appl. Soil Ecol.*, 46, 436-442, 2010.

1086 Guimberteau, M., Drapeau, G., Ronchail, J., Sultan, B., Polcher, J., Martinez, J. M., Prigent, C., Guyot, J. L.,
1087 Cochonneau, G., Espinoza, J. C., Filizola, N., Fraizy, P., Lavado, W., De Oliveira, E., Pombosa, R., Noriega,
1088 L., and Vauchel, P.: Discharge simulation in the sub-basins of the Amazon using ORCHIDEE forced by new
1089 datasets. *Hydrol. Earth Syst. Sci.*, 16, 911-935, 2012.

1090 Guimberteau, M., Zhu, D., Maignan, F., Huang, Y., Yue, C., Dantec-Nédélec, S., Otlé, C., Jornet-Puig, A., Bastos,
1091 A., Laurent, P., Goll, D., Bowring, S., Chang, J., Guenet, B., Tifafi, M., Peng, S., Krinner, G., Ducharne, A.,
1092 Wang, F., Wang, T., Wang, X., Wang, Y., Yin, Z., Lauerwald, R., Joetzjer, E., Qiu, C., Kim, H., and Ciais, P.:
1093 ORCHIDEE-MICT (revision 4126), a land surface model for the high-latitudes: model description and
1094 validation. *Geosci. Model Dev.*, 11, 121-163, 2018.

1095 Hanson, P. C., Hamilton, D. P., Stanley, E. H., Preston, N., Langman, O. C., and Kara, E. L.: Fate of allochthonous
1096 dissolved organic carbon in lakes: a quantitative approach. *PLoS One*, 6, e21884, 2011.

1097 Haregeweyn, N., Poesen, J., Deckers, J., Nyssen, J., Haile, M., Govers, G., Verstraeten, G., and Moeyersons, J.:
1098 Sediment-bound nutrient export from micro-dam catchments in Northern Ethiopia. *Land Degrad. Dev.*, 19,
1099 136-152, 2008.

1100 Hartmann, J., Lauerwald, R., and Moosdorf, N.: GLORICH - Global river chemistry database, in: PANGAEA (Ed.),
1101 2019.

1102 Hengl, T., de Jesus, J. M., MacMillan, R. A., Batjes, N. H., Heuvelink, G. B., Ribeiro, E., Samuel-Rosa, A.,
1103 Kempen, B., Leenaars, J. G., Walsh, M. G., and Gonzalez, M. R.: SoilGrids1km--global soil information based
1104 on automated mapping. *PLoS One*, 9, e105992, 2014.

1105 Hu, Y., Kuhn, N. J.: Erosion-induced exposure of SOC to mineralization in aggregated sediment. *Catena*, 137, 517-
1106 525, 2016.

1107 Hoffmann, T. O.: 9.20 - Carbon Sequestration on Floodplains, in: *Treatise on Geomorphology (Second Edition)*,
1108 edited by: Shroder, J. F., Academic Press, Cambridge, Massachusetts, United States, 10, 458-477, 2022,

1109 <https://doi.org/10.1016/B978-0-12-818234-5.00069-9>.

1110 Hoffmann, T. O., Baulig, Y., Fischer, H., and Blöthe, J.: Scale breaks of suspended sediment rating in large rivers in
1111 Germany induced by organic matter. *Earth Surf. Dynam.*, 8, 661–678, 2020

1112 Hoffmann, T., Schlummer, M., Notebaert B., Verstraeten, G., and Korup, O.: Carbon burial in soil sediments from
1113 Holocene agricultural erosion, Central Europe. *Glob. Biogeochem. Cy.*, 27, 828-835, 2013.

1114 Janssens, I. A., Freibauer, A., Ciais, P., Smith, P., Nabuurs, G. J., Folberth, G., Schlamadinger, B., Hutjes, R. W.,
1115 Ceulemans, R., Schulze, E. D., Valentini, R., and Dolman, A. J.: Europe's terrestrial biosphere absorbs 7 to
1116 12% of European anthropogenic CO₂ emissions. *Science*, 300, 1538-1542, 2003.

1117 Jetten, V., Govers, G., Hessel, R.: Erosion models: quality of spatial predictions. *Hydrol. Process.*, 17, 887-900,
1118 2003.

1119 Kalbitz, K., Schmerwitz, J., Schwesig, D., and Matzner, E.: Biodegradation of soil-derived dissolved organic matter
1120 as related to its properties. *Geoderma*, 113, 273-291, 2003.

1121 Knapp, A. K., Briggs, J. M., and Koelliker, J. K.: Frequency and Extent of Water Limitation to Primary Production
1122 in a Mesic Temperate Grassland. *Ecosystems*, 4, 19-28, 2001.

1123 Krinner, G., Viovy, N., de Noblet-Ducoudré, N., Ogée, J., Polcher, J., Friedlingstein, P., Ciais, P., Sitch, S., and
1124 Prentice, I. C.: A dynamic global vegetation model for studies of the coupled atmosphere-biosphere system.
1125 *Global Biogeochem. Cycles*, 19, 2005.

1126 Lal, R.: Soil erosion and the global carbon budget. *Environ. Int.*, 29, 437-450, 2003.

1127 Lal, R.: Soil carbon sequestration impacts on global climate change and food security. *Science*, 304, 1623-1627,
1128 2004.

1129 Lauerwald, R., Laruelle, G., Hartmann, J., Ciais, P., and Regnier, P.: Spatial patterns in CO₂ evasion from the global
1130 river network: Spatial patten of riverine pCO₂ and FCO₂. *Global Biogeochem. Cycles*, 29, 2015.

1131 Lauerwald, R., Regnier, P., Camino-Serrano, M., Guenet, B., Guimberteau, M., Ducharne, A., Polcher, J., and Ciais,
1132 P.: ORCHILEAK (revision 3875): a new model branch to simulate carbon transfers along the terrestrial–
1133 aquatic continuum of the Amazon basin. *Geosci. Model Dev.*, 10, 3821-3859, 2017.

1134 Lauerwald, R., Regnier, P., Guenet, B., Friedlingstein, P., and Ciais, P.: How Simulations of the Land Carbon Sink
1135 Are Biased by Ignoring Fluvial Carbon Transfers: A Case Study for the Amazon Basin. *One Earth*, 3, 226-236,
1136 2020.

1137 Lehner, B., Verdin, K., and Jarvis, A.: New global hydrography derived from spaceborne elevation data. *Eos*,
1138 *Transactions, AGU*, 89, 93-94, 2008.

1139 Lugato, E., Paustian, K., Panagos, P., Jones, A., and Borrelli, P.: Quantifying the erosion effect on current carbon
1140 budget of European agricultural soils at high spatial resolution. *Glob. Change Biol.*, 22, 1976-1984, 2016.

1141 Luo, X., Li, H., Leung L.R., Tesfa, T. K., Getirana, A., Papa, F., and Hess L. L.: Modeling surface water dynamics
1142 in the Amazon Basin using MOSART-Inundation v1.0: impacts of geomorphological parameters and river flow
1143 representation. *Geosci. Model Dev.*, 10, 1233-1259, 2017.

1144 Maavara, T., Lauerwald, R., Regnier, P., and Van Cappellen, P.: Global perturbation of organic carbon cycling by
1145 river damming. *Nat. Commun.*, 8, 15347, 2017.

1146 Mei, X., Van Gelder, P., Dai, Z., and Tang, Z.: Impact of dams on flood occurrence of selected rivers in the United
1147 States. *Front. Earth Sci.*, 11, 268-282, 2016.

1148 Meybeck, M.: Riverine transport of atmospheric carbon: sources, global typology and budget. *Water Air Soil*
1149 *Pollut.*, 70, 443-463, 1993.

1150 Molinas, A., and Wu, B.: Transport of sediment in large sand-bed rivers. *J. Hydraul. Res.*, 39, 135-146, 2001.

1151 Moore, I. D., and Wilson, J. P.: Length-slope factors for the Revised Universal Soil Loss Equation: Simplified
1152 method of estimation. *J. Soil Water Conserv.*, 47, 423-428, 1992.

1153 Nadeu, E., de Vente, J., Martínez-Mena, M., and Boix-Fayos, C.: Exploring particle size distribution and organic
1154 carbon pools mobilized by different erosion processes at the catchment scale. *J. Soils Sediments*, 11, 667-678,
1155 2011.

1156 Naipal, V., Lauerwald, R., Ciais, P., Guenet, B., and Wang, Y.: CE-DYNAM (v1): a spatially explicit process-based
1157 carbon erosion scheme for use in Earth system models. *Geosci. Model Dev.*, 13, 1201-1222, 2020.

1158 Nakhavali, M., Lauerwald, R., Regnier, P., Guenet, B., Chadburn, S., and Friedlingstein, P.: Leaching of dissolved
1159 organic carbon from mineral soils plays a significant role in the terrestrial carbon balance. *Glob. Change Biol.*,
1160 27, 1083-1096, 2021.

1161 Nardi, F., Annis, A., Di Baldassarre, G., Vivoni, E.R., and Grimaldi, S.: GFPLAIN250m, a global high-resolution
1162 dataset of Earth's floodplains. *Sci. Data*, 6, 180309, 2019.

1163 Nearing, M. A., Foster, G. R., Lane, L. J., and Finkner, S. C.: A Process-Based Soil Erosion Model for USDA-
1164 Water Erosion Prediction Project Technology. *Transactions of the Asae*, 32, 1587-1593, 1989.

1165 Neckles, H. A. and Neill, C.: Hydrologic control of litter decomposition in seasonally flooded prairie marshes.
1166 *Hydrobiologia*, 286, 155-165, 1994.

1167 Neitsch, S. L., Williams, J. R., Arnold, J. G., and Kiniry, J. R.: Soil and Water Assessment Tool Theoretical
1168 Documentation Version 2009. Texas Water Resources Institute, College Station, 2011.

1169 Nie, X., Li, Z., He, J., Huang, J., Zhang, Y., Huang, B., Ma, W., Lu, Y., and Zeng, G.: Enrichment of organic carbon
1170 in sediment under field simulated rainfall experiments. *Environ. Earth Sci.*, 74, 5417-5425, 2015.

1171 Nodvin, S. C., Driscoll, C. T., and Likens, G. E.: Simple partitioning of anions and dissolved organic carbon in a
1172 forest soil. *Soil Sci.*, 142, 27-35, 1986.

1173 Nunes, A. N., de Almeida, A. C., and Coelho, C. O. A.: (2011) Impacts of land use and cover type on runoff and soil
1174 erosion in a marginal area of Portugal. *Appl. Geogr.*, 31, 687-699, 2011.

1175 Oeurng, C., Sauvage, S., and Sánchez-Pérez, J. M.: Assessment of hydrology, sediment and particulate organic
1176 carbon yield in a large agricultural catchment using the SWAT model. *J. Hydrol.*, 401, 145-153, 2011.

1177 Parton, W. J., Schimel, D. S., Cole, C. V., and Ojima, D. S.: Analysis of Factors Controlling Soil Organic Matter
1178 Levels in Great Plains Grasslands1. *Soil Sci. Soc. Am. J.*, 51, 1173-1179, 1987.

1179 Parton, W. J., Stewart, J. W. B., and Cole, C. V.: Dynamics of C, N, P and S in grassland soils: a model.
1180 *Biogeochemistry*, 5, 109-131, 1988.

1181 Polyakov, V. O., and Lal, R.: Soil organic matter and CO₂ emission as affected by water erosion on field runoff
1182 plots. *Geoderma*, 143, 216-222, 2008.

1183 Quine, T. A.: An investigation of spatial variation in soil erosion, soil properties and crop production with an
1184 agricultural field in Devon, UK. *J. Soil Water Conserv.*, 57, 55-65, 2002.

1185 Quinton, J. N., Govers, G., Van Oost, K., and Bardgett, R. D.: The impact of agricultural soil erosion on
1186 biogeochemical cycling. *Nat. Geosci.*, 3, 311-314, 2010.

1187 Raymond, P. A., Hartmann, J., Lauerwald, R., Sobek, S., McDonald, C., Hoover, M., Butman, D., Striegl, R.,
1188 Mayorga, E., Humborg, C., Kortelainen, P., Durr, H., Meybeck, M., Ciais, P., and Guth, P.: Global carbon
1189 dioxide emissions from inland waters. *Nature*, 503, 355-359, 2013.

1190 Reddy, K. R., Patrick Jr, and W. H.: Effect of alternate aerobic and anaerobic conditions on redox potential, organic
1191 matter decomposition and nitrogen loss in a flooded soil. *Soil Biol. Biochem.*, 7, 87-94, 1975.

1192 Regnier, P., Friedlingstein, P., Ciais, P., Mackenzie, F. T., Gruber, N., Janssens, I. A., Laruelle, G. G., Lauerwald,
1193 R., Luyssaert, S., Andersson, A. J., Arndt, S., Arnosti, C., Borges, A. V., Dale, A. W., Gallego-Sala, A.,
1194 Godd ris, Y., Goossens, N., Hartmann, J., Heinze, C., Ilyina, T., Joos, F., LaRowe, D. E., Leifeld, J., Meysman,
1195 F. J. R., Munhoven, G., Raymond, P. A., Spahni, R., Suntharalingam, P., and Thullner, M.: Anthropogenic
1196 perturbation of the carbon fluxes from land to ocean. *Nat. Geosci.*, 6, 597-607, 2013.

1197 Reynolds, C., Jackson, T., and Rawls, W.: Estimating available water content by linking the FAO soil map of the
1198 world with global soil profile databases and pedo-transfer functions, *Am. Geophys. Union Fall Meet. EOS*
1199 *Trans. Spring Meet. Suppl.*, 80, S132, 1999.

1200 Sanderman, J., Hengl, T., and Fiske, G. J.: Soil carbon debt of 12,000 years of human land use. *Proc. Natl. Acad.*
1201 *Sci.*, 114, 9575-9580, 2017.

1202 Schneider, C., Fl rke, M., Eisner, E., and Voss, F.: Large scale modelling of bankfull flow: An example for Europe.
1203 *J. Hydrol.*, 408, 235-245, 2011.

1204 Shanguan, W., Dai, Y., Duan, Q., Liu, B., and Yuan, H.: A global soil data set for earth system modeling. *J. Adv.*
1205 *Model. Earth Syst.*, 6, 249-263, 2014.

1206 Sharpley, A. N., and Williams, J. R.: EPIC-erosion/productivity impact calculator: 2. User manual. Technical
1207 Bulletin - United States Department of Agriculture, 4, 206-207, 1990.

1208 Smith, S. V., Renwick, W. H., Buddemeier, R. W., and Crossland, C.J.: Budgets of soil erosion and deposition for
1209 sediments and sedimentary organic carbon across the conterminous United States. *Global Biogeochem. Cycles*,
1210 15, 697-707, 2001.

1211 Stallard, R. F.: Terrestrial sedimentation and the carbon cycle: Coupling weathering and erosion to carbon burial.
1212 *Global Biogeochem. Cycles*, 12, 231-257, 1998.

1213 Stocker, B. D., Zscheischler, J., Keenan, T. F., Prentice, I. C., Seneviratne, S. I., and Pe uelas, J.: Drought impacts
1214 on terrestrial primary production underestimated by satellite monitoring. *Nat. Geosci.*, 12, 264-270, 2019.

1215 Telmer, K., and Veizer, J.: Carbon fluxes, pCO₂ and substrate weathering in a large northern river basin, Canada:
1216 carbon isotope perspectives. *Chem. Geol.*, 159, 61-86, 1999.

1217 Tian, H., Yang, Q., Najjar, R. G., Ren, W., Friedrichs, M. A. M., Hopkinson, C. S., and Pan, S.: Anthropogenic and
1218 climatic influences on carbon fluxes from eastern North America to the Atlantic Ocean: A process-based
1219 modeling study. *J. Geophys. Res.: Biogeosci.*, 120, 757-772, 2015.

- 1220 Timpe, K., and Kaplan, D.: The changing hydrology of a dammed Amazon. *Sci. Adv.*, 3, 11, e1700611, 2017.
- 1221 Van Hemelryck, H., Govers, G., Van Oost, K., and Merckx, R.: Evaluating the impact of soil redistribution on the in
1222 situ mineralization of soil organic carbon. *Earth Surf. Process. Landf.*, 36, 427-438, 2011.
- 1223 Van Oost, K., Quine, T. A., Govers, G., De Gryze, S., Six, J., Harden, J. W., Ritchie, J. C., McCarty, G. W.,
1224 Heckrath, G., Kosmas, C., Giraldez, J. V., da Silva, J. R., and Merckx, R.: The impact of agricultural soil
1225 erosion on the global carbon cycle. *Science*, 318, 626-629, 2007.
- 1226 Vigiak, O., Malago, A., Bouraoui, F., Vanmaercke, M., Obreja, F., Poesen, J., Habersack, H., Feher, J., and Groselj,
1227 S.: Modelling sediment fluxes in the Danube River Basin with SWAT. *Sci. Total Environ.*, 599-600, 992-1012,
1228 2017.
- 1229 Vörösmarty, C. J., Fekete, B. M., Meybeck, M., and Lammers, R. B.: Geomorphometric attributes of the global
1230 system of rivers at 30-minute spatial resolution. *J. Hydrol.*, 237, 17-39, 2000.
- 1231 Wang, X., Cammeraat, E. L., Romeijn, P., and Kalbitz, K.: Soil organic carbon redistribution by water erosion--the
1232 role of CO₂ emissions for the carbon budget. *PLoS One*, 9, e96299, 2014a.
- 1233 Wang, Z., Govers, G., Steegen, A., Clymans, W., Van den Putte, A., Langhans, C., Merckx, R., and Van Oost, K.:
1234 Catchment-scale carbon redistribution and delivery by water erosion in an intensively cultivated area.
1235 *Geomorphology*, 124, 65-74, 2010.
- 1236 Wang, Z., Hoffmann, T., Six, J., Kaplan, J. O., Govers, G., Doetterl, S., and Van Oost, K.: Human-induced erosion
1237 has offset one-third of carbon emissions from land cover change. *Nat. Clim. Chang.*, 7, 345-349, 2017.
- 1238 Wang, Z., Van Oost, K., and Govers, G.: Predicting the long-term fate of buried organic carbon in colluvial soils.
1239 *Global Biogeochem. Cycles*, 29, 65-79, 2015.
- 1240 Wang, Z., Van Oost, K., Lang, A., Quine, T., Clymans, W., Merckx, R., Notebaert, B., and Govers, G.: The fate of
1241 buried organic carbon in colluvial soils: a long-term perspective. *Biogeosciences*, 11, 873-883, 2014b.
- 1242 Xu, X., Sherry, R. A., Niu, S., Li, D., and Luo, Y.: Net primary productivity and rain-use efficiency as affected by
1243 warming, altered precipitation, and clipping in a mixed-grass prairie. *Glob. Change Biol.*, 19, 2753-2764, 2013.
- 1244 Yamazaki, D., Kanae, S., Kim, H., and Oki T.: A physically based description of floodplain inundation dynamics in
1245 a global river routing model. *Water Resour. Res.*, 47, W04501, doi:10.1029/2010WR009726, 2011.
- 1246 Zhang, H., Lauerwald, R., Regnier, P., Ciais, P., Yuan, W., Naipal, V., Guenet, B., Van Oost, K., and Camino-
1247 Serrano, M.: Simulating Erosion-Induced Soil and Carbon Delivery From Uplands to Rivers in a Global Land
1248 Surface Model. *J. Adv. Model. Earth Syst.*, 12, e2020MS002121, 2020.
- 1249 Zhang, H., Liu, S., Yuan, W., Dong, W., Xia, J., Cao, Y., and Jia, Y.: Loess Plateau check dams can potentially
1250 sequester eroded soil organic carbon. *J. Geophys. Res. Biogeosci.*, 121, 2016.
- 1251 Zhang, H., Liu, S., Yuan, W., Dong, W., Ye, A., Xie, X., Chen, Y., Liu, D., Cai, W., and Mao, Y.: Inclusion of soil
1252 carbon lateral movement alters terrestrial carbon budget in China. *Sci. Rep.*, 4, 7247, 2014.